Final Report

U.S. DOT
Pipeline and Hazardous Materials Safety Administration

Competitive Academic Agreement Program

Toward Permanently Installed Pipeline Monitoring Systems

The Research Foundation for SUNY on behalf of the University at Buffalo

Executive Summary

The present report summarizes the activities and results obtained during work under contract no. DTPH56-13-H-CAAP03 by University at Buffalo.

The team has investigated the use of a built-in monitoring system based on permanently installed low profile piezoelectric transducers which have the capability of transmitting and receiving guided ultrasonic waves (GUWs) over the length of a pipeline. Advanced signal processing algorithms based on probabilistic concepts have been developed to perform the critical tasks of: 1) damage localization (e.g., leaks), and 2) damage characterization (e.g., thickness map)

The main advantage of this approach, compared to conventional GUWs approaches, is that the algorithms can take into account uncertainty in sensor measurements to reliably locate and quantify corrosion damage. Hence the approach is attractive for field applications where uncertainties in sensor measurements, caused not only by the sensor impreciseness and noise, but also from the multimode and dispersive nature of GUWs, may hamper their reliability in terms of automatic damage detection. The proposed system could operate in two modes. Under mode 1 (i.e., active mode), the system will be activated for periodically scheduled inspections. Under mode 2, (i.e., passive mode) the system will continuously monitor the damage progression. It is envisioned that the proposed system will provide an "early warning" of the corrosion process and allow for the planning and implementation of mitigation strategies at a point where it is less expensive and invasive than when the structural performance of the pipeline has been seriously compromised.

The first part of this report illustrates the basis of the technical approach considered for the active mode (i.e., wall thickness mapping). The second part of this report illustrates the basis of the technical approach considered for the passive mode (e.g. leaks detections).

Table of Contents

1. INTRODUCTION 5

1.1. BACKGROUND 5

1.2. OBJECTIVE 6

2. WALL THICKNESS TOMOGRAPHY 7

2.1. OVERVIEW 7

2.2. DETERMINING THICKNESS LOSS REGIONS 8

2.2.1. Helical Waves in Cylindrical Structures 8

2.2.2. Relative position of transducer pairs 11

2.2.3. Wave velocity 13

2.2.4. Probabilistic reconstruction algorithm 15

2.2.5. Experimental Results 17

2.3. QUANTITATIVE THICKNESS LOSS EVALUATION 30

2.3.1. Corrosion patch quantification 30

2.3.2. Experimental results 36

2.4. SUMMARY 42

3. ACOUSTIC EMISSION LOCALIZATION 43

3.1. OVERVIEW 43

3.2. SOURCE LOCALIZATION IN CYLINDRICAL SHELLS 44

3.2.1. Geodesic analysis 44

3.2.2. Time-of-flight measurement 47

3.3. PROBABILITY ZONE DETERMINATION OF AE SOURCE 48

3.3.1. Uncertainty propagation based on Unscented Transform 48

3.3.2. Confidence quantification 50

3.3.3. Numerical evaluation 50

3.4. EXPERIMENTAL TESTING 52

3.4.1. Setup of experiment 52

3.4.2. Results 54

3.5. SUMMARY 58

4. BROADER IMPACTS 58

5. CONCLUSIONS 60

6. REFERENCES 61

List of Figures

FIG. 1 A large number of the lowest order helical paths existing between a transmitting/receiving pair of transducer sensors on a cylindrical shell. Sensors are labeled S_i,S_j, and are marked in yellow. The first order path is marked by a dashed red line. 9

FIG. 2 The three lowest order helical paths between a transmitting/receiving pair of transducer sensors on a cylindrical shell. Paths are labeled in order as $l_{1,2,3}$. The theoretical cut line where the structure is "unwrapped" is also shown. 10

FIG. 3 "Unwrapped" plate representation of the cylindrical shell shown in Fig. 2. Higher order helical paths are shown being received at "virtual" sensors. 10

FIG. 4 Contour of the separation coefficient, κ, for the first two helical paths. Contour levels are given based on transducer placement parameters, β and δ. 12

FIG. 5 Phase (left) and group (right) velocity across the frequency-thickness product. The shaded area shows the range of low dispersivity in the A_0 and S_0 mode group velocity. 14

FIG. 6 Steel pipe experimental setup and data acquisition system. PZT sensors are labeled $S_{1,2,...,6}$. 19

FIG. 7 Three cases of simulated corrosion (thickness reduction) in the steel pipe of Fig. 6. 20

FIG. 8 Schematic view of the sensor network and simulated corrosion. 20

FIG. 9 Schematic of the first six helical paths between sensors S1 and S3. 22

FIG. 10 Received signals for the baseline and damaged case. 23

FIG. 11 Differential signal for the baseline and damaged states shown in Fig. 10. 24

FIG. 12 Damage sensitive feature values for the 12 sensor pair for the first nine helical orders. 24

FIG. 13 1st, 3rd, and 9th helical paths between all sensor pairs. Left: Cylinder. Right: Unwrapped representation. 25

FIG. 14 Image reconstruction of thickness loss due to damage case I. Left: cylindrical structure. Right: unwrapped representation of the cylinder. 26

FIG. 15 Fifth order helical paths for the 12 sensor pairs listed in Table I. 28

FIG. 16 Damage sensitive features for the 12 sensor pairs at the four operational frequencies listed in Table III. 29

FIG. 17 Image reconstructions of thickness loss for damage cases II and III. Left: cylindrical structure. Right: unwrapped representation of the cylinder. 30

FIG. 18 Schematic of a corrosion patch between a pair of sensors and the corresponding image intensity. 31

FIG. 19 Group velocity dispersion curves for the A_0 and S_0 wave modes. Shaded areas indicate low dispersivity. Thickened lines indicate high dispersivity. 32

FIG. 20 Algorithm logic for the image reconstruction approach to estimating thickness loss..... 36

FIG. 21 Image reconstruction of thickness loss regions for damage cases I, II, and III..... 37

FIG. 22 Image intensity contour levels for damage case I. 38

FIG. 23 Example of a contour level of $\gamma = 0.71$ for damage case I. 39

FIG. 24 Error in objective function on a logarithmic scale for different trial values of group velocity and γ 39

FIG. 25 Quantitative corrosion patch monitoring results for damage cases I, II, and III. 42

FIG. 26 Triangulation of an acoustic emission source in a cylindrical shell using three sensors. 44

FIG. 27 Unwrapped view representation of the outer pipe surface. 45

FIG. 28 AE source localization sequence. 47

FIG. 29 Visualization of the Unscented Transform sampling algorithm..... 52

FIG. 30 Monte Carlo simulation using a statistically significant number of sample points..... 52

FIG. 31 Arrangement of transducer sensors (left), and pipe and layout of processing tools (right). 53

FIG. 32 Layout of sensor locations on the unwrapped grid view of the pipe surface. 54

FIG. 33 Plots of mean estimates and 90% confidence ellipses for 11 simulated AE sources. 55

FIG. 34 Enhanced image of the estimation components for AE source #8. 56

FIG. 35 Kullback-Leibler divergence for each AE location, comparing the UT method to a Monte Carlo simulation. 57

FIG. 36 CIE 680 project presentation slide. 59

1. INTRODUCTION

1.1. Background

Pipelines transport nearly all crucial energy sources throughout the nation. After the pipe has been in operation for some time, in areas lacking adequate protection, the corrosion processes start on the interior or exterior (or both) surfaces of the pipe. Corrosion leads to cracks that reduce the strength of the pipe yielding to wall breaks, which, in turn, cause leaks or bursts.

Several nondestructive evaluation (NDE) techniques have been developed for evaluating the condition of pipelines. These techniques can be largely divided according to the physical phenomenon they exploit: electromagnetic, ultrasound, and acoustics. Although NDE techniques have seen significant development, their primary disadvantage is that the sensing mechanism is typically only installed temporarily. This installation method poses two problems. First, the testing is only performed at scheduled intervals because the sensing mechanism is not permanently available. However, with short time-scale events, such as excavation or an earthquake, the testing schedule may allow the pipeline to operate under dangerous conditions, as demonstrated with the excavation damage which led to the explosion that occurred on June 10, 1999 in Bellingham, Washington and in Carlsbad, NM, which resulted in a total of 15 deaths and property and other damages totaling about $46 million. The second complication from temporary sensor installation arises from the need to obtain direct access to the structure to perform the NDE. Because pipelines are typically installed underground, direct access to the pipeline might require extensive excavation. In urban areas, this excavation process can become especially expensive if access to the pipeline requires digging beneath a roadway. Furthermore, the excavation process itself may cause damage to the pipeline. Another major disadvantage of many current NDE techniques is that, depending on the particular technique used, they require that the pipeline be taken temporarily out of service. This aspect of the testing increases the potential cost of NDE techniques. Consequently, conventional nondestructive evaluation (NDE) methods have moved towards a more comprehensive concept, called Structural Health Monitoring (SHM). A SHM system, by fitting the pipe with their own sensing and analysis system can provide real-time and rapid assessment of damage to pipelines after natural disasters, such as earthquakes. This is essential for

early emergency response, efficient preparation of rescue plans, and mitigation of the disastrous consequences.

Structural Health Monitoring (SHM) by guided ultrasonic waves (GUWs) is a field that has received significant interest over the past few years and has led to the development of a wide variety of systems and signal processing techniques for the damage assessment of pipelines. The advantages of this technique include: (1) the use of transducers that can be permanently attached to the structural element to perform real-time monitoring and routine inspection with the same sensing system, (2) the ability to probe a large area of the structure, locating cracks and notches from only a few monitoring points and (3) the capability to detect both active cracks and pre-existing cracks by toggling between the modes of "passive" acoustic emission testing and "active" ultrasonic testing.

Despite these novel SHM systems seeing significant developments, their reliability has been questioned. One of the main culprits in unreliable results is the inherent uncertainty in sensor measurements. The uncertainties in sensor measurements are caused not only by the sensor impreciseness and noise, but also manifest themselves from the ambiguities and inconsistencies present within the environment, and from an inability to distinguish between them. Sensing systems available in civil infrastructures, (e.g., strain gages, piezoelectric sensors, optic fiber sensors) produce large quantities of raw signaling that exhibit hidden correlations, are distorted by noise, but still retain features tied to their particular physical origin (e.g., damage).

1.2. Objective

To overcome these limitations, a built-in monitoring system based on permanently installed low profile piezoelectric transducers which have the capability of transmitting and receiving guided ultrasonic waves (GUWs) over the length of a pipeline, is investigated in this research. Advanced signal processing algorithms based on probabilistic concepts will be developed to perform the critical tasks of 1) <u>damage localization</u> and 2) <u>damage characterization</u>. The proposed system will operate in two modes. Under mode 1, the system will continuously monitor the damage progression. Under mode 2, the system will be activated for periodically scheduled inspections. It is envisioned that the proposed system will provide an "early warning" of the corrosion process and allow for the planning and implementation of mitigation strategies at a point where it is less

expensive and invasive than when the structural performance of the pipeline has been seriously compromised.

2. WALL THICKNESS TOMOGRAPHY

2.1. Overview

In recent years, many efforts have been made to combine GUWs and imaging reconstruction algorithms for the structural diagnosis of complex structures [1]–[7]. For example, Leonard and Hinders [5], [6] implemented GUW tomography on pipes by treating them as Lamb waves that propagate around the structure along various helical paths (see Fig. 1). They designed an experimental apparatus to mimic two circumferential belts of transducers [5] (helical ultrasound tomography, HUT) and a single line of transducers along the meridian of the cylindrical surface [6] (meridional ultrasonic tomography, MUT). While both approaches (i.e., HUT and MUT) shown potential to identify corrosion-type defects or flaws, good quality images can be obtained by using a dense array of transducers and iteratively reconstructing the image in pixel level; this aspect can increase the computational cost of iterative-based reconstruction algorithms. Furthermore, they used only the first arriving helical mode (i.e., red dashed line in Fig. 1) in the tomographic reconstruction algorithm, neglecting the contributions of other arrivals from different helical paths (i.e., solid blue lines in Fig. 1).

Recently, electro acoustic magnetic transducers were used by Nagy, et al. [1] for corrosion monitoring in plates and pipes. In their work the fundamental antisymmetric A_0 Lamb wave mode was used, in the so-called constant group velocity (CGV) region, to exploit the advantage of constant group velocity and high sensitivity to thickness loss, due to dispersive phase velocity. Cawley, et al. [2] proposed an inspection strategy based on a permanently installed corrosion monitoring system. High resolution short-range guided wave tomography based on the hybrid algorithm for robust breast ultrasound tomography (HARBUT) was developed by Huthwaite, et al. [8] to map wall thickness losses. The first and second order helical waves were excited and received using electro acoustic magnetic transducers by Willey, et al. [3] for improving image resolution and thickness measurement accuracy. Despite these GUW-based tomography

approaches having seen significant developments, their primary disadvantage is that a large sensor density (or number of transducers) is usually required in order to obtain a sufficient ray density and, ultimately, high resolution.

Here, we introduce a multi-helical ultrasonic imaging (MHUI) approach for the structural health monitoring (SHM) of cylindrical shell structures. The approach uses an array of six permanently installed low profile piezoelectric transducers to generate and receive high order helical guided waves (up to ninth order) around the cylindrical structure. This method artificially increases the ray density/image resolution without increasing the number of sensors. An iterative-free image reconstruction algorithm, capable for taking into account the contribution of many helical waves, is proposed in order to detect and localize defects, such as pipe wall thickness losses. This section is divided into two main parts: 1) Mapping local areas of thickness loss, and 2) Quantitative evaluation of remaining wall thickness.

2.2. Determining Thickness Loss Regions

2.2.1. Helical Waves in Cylindrical Structures

Consider a cylindrical structure instrumented with a pair of transmitting/receiving (S_i/S_j) transducers, as shown in Fig. 1. On cylindrical structures, circumferential waves can propagate from the transmitter S_i to the receiver S_j through an infinite number of helical paths [9], [7]. Here, the term "*h*-th order" helical path is used to indicate the *h*-th longest path between a transducer pair, (the first order helical path represents the shortest path). Fig. 1 demonstrates a large number of helical paths between a pair of sensors on a cylindrical shell. In Fig. 2, the first three helical paths between a pair of sensors are shown.

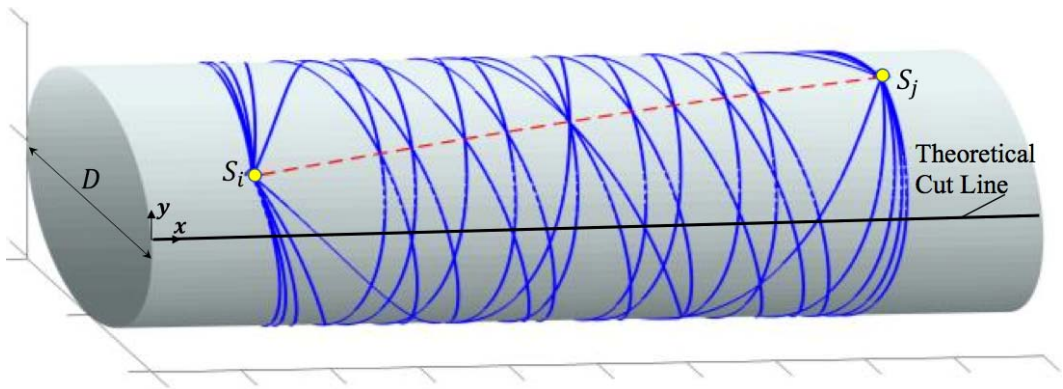

FIG. 1 A large number of the lowest order helical paths existing between a transmitting/receiving pair of transducer sensors on a cylindrical shell. Sensors are labeled S_i,S_j, and are marked in yellow. The first order path is marked by a dashed red line.

For curved structures with a small thickness-to-diameter ratio, these circumferential waves may be approximated by Lamb waves. This is facilitated by replacing the cylindrical shell with an equivalent "unwrapped" plate [9], [7], where the guided waves in the curved shell are approximated by the plate waves in unwrapped plate.

Using the unwrapped representation, each helical wave can be treated as a single waveform detected by multiple "virtual" transducers placed at vertically repeating positions [5], as shown in Fig. 3. The adoption of the "virtual" sensor representation is simply one method of handling the multiple arrivals of the same excitation at the receiving sensor S_j. The vertical distance between each pair of virtual transducers is $n_h \pi D$, where D is the diameter of the cylinder, and $n_h = 0, -1, +1, -2, +2, \ldots, -\infty, +\infty$.

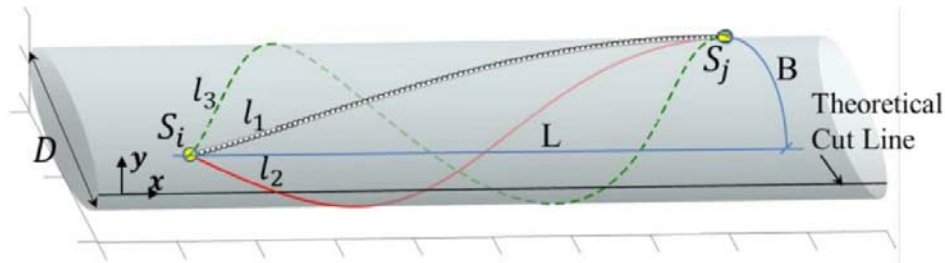

FIG. 2 The three lowest order helical paths between a transmitting/receiving pair of transducer sensors on a cylindrical shell. Paths are labeled in order as $l_{1,2,3}$. The theoretical cut line where the structure is "unwrapped" is also shown.

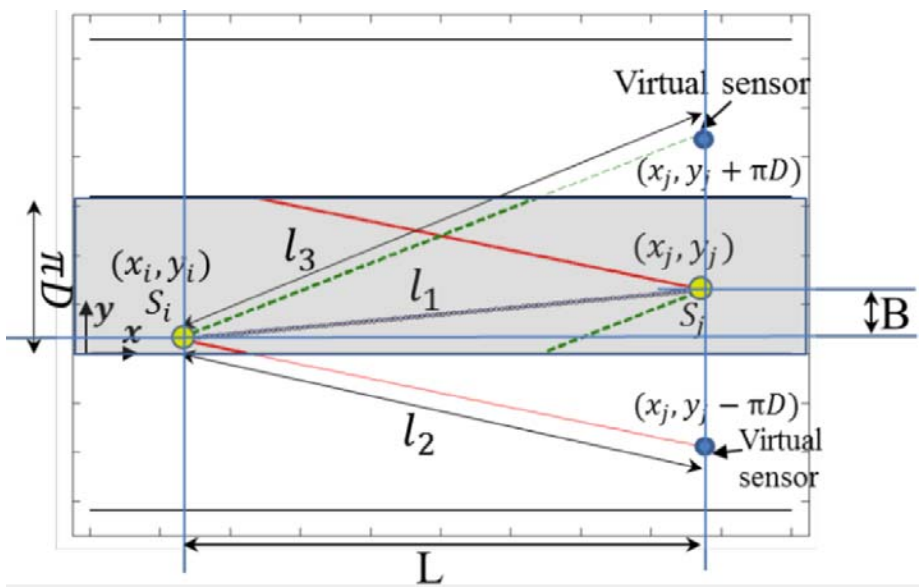

FIG. 3 "Unwrapped" plate representation of the cylindrical shell shown in Fig. 2. Higher order helical paths are shown being received at "virtual" sensors.

Given a transducer pair located at the coordinates (x_i, y_i) and (x_j, y_j), the length of the h-th order helical path l_h can be calculated as:

$$l_h = \sqrt{(L)^2 + \left(B + n_h \pi D\right)^2}\ , \quad n_h = 0, \pm 1, \pm 2, \ldots, \pm\infty \tag{1}$$

where $L = |x_j - x_i|$ and $B = |y_j - y_i|$. The theoretical cut line can be chosen to satisfy the inequality $B \leq \pi D / 2$, without any loss of generality. Eq. (1) represents a set of lengths (l_h) sorted from the smallest path l_1 to the largest path l_h.

The time of arrival $t_h^{(m)}$ of each helical Lamb-like mode depends upon both its group velocity $V_g^{(m)}$ and the helical path length as:

$$t_h^{(m)} = \frac{l_h}{V_g^{(m)}} \tag{2}$$

where the superscript *m* is used to indicate the specific Lamb wave mode propagating along the *h*-th helical path. As per Eq. (2), the time of arrival $t_h^{(m)}$ of each helical mode can be controlled by two parameters; that is, the relative position of the transducers and the wave velocity. These two parameters are discussed in the following sections.

2.2.2. Relative position of transducer pairs

Consider a non-dispersive Lamb-like guided wave mode propagating along two consecutive helical paths, *h* and $h-1$ in helical order. The fact that the wave is non-dispersive means that its velocity does not vary for a small change in frequency. Under this assumption of non-dispersivity, the group velocity $V_g^{(m)}$ of the *m* wave mode may be considered constant. The time difference between the two consecutive arrivals of the wave mode may then be estimated as:

$$\Delta t_{h-1,h}^{(m)} = \frac{l_h}{V_g^{(m)}} - \frac{l_{h-1}}{V_g^{(m)}} \tag{3}$$

Substituting Eq. (1) into Eq. (2), the following relation may be obtained:

$$\Delta t_{h,h-1}^{(m)} = \frac{L}{V_g^{(m)}} \kappa_{h,h-1} \tag{4}$$

where the coefficient $\kappa_{h,h-1}$ (termed here the "separation coefficient") is defined as:

$$\kappa_{h,h-1} = (\sqrt{1+(\beta+n_h\pi\delta)^2} - \sqrt{1+(\beta+n_{h-1}\pi\delta)^2}), \quad n = 0, \pm 1, \pm 2, \ldots, \pm\infty \tag{5}$$

In Eq. (5), $\beta = B/L$ and $\delta = D/L$ are each dimensionless quantities and are associated with the relative position between the two transducers. Fig. 4 shows a contour plot of the separation coefficient $\kappa_{h,h-1}$ versus δ and β for the first two helical orders, $h = 2$ and $h-1 = 1$.

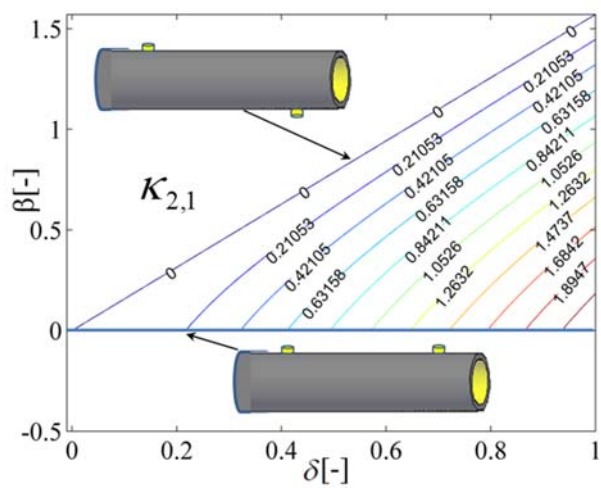

FIG. 4 Contour of the separation coefficient, κ, for the first two helical paths. Contour levels are given based on transducer placement parameters, β and δ.

A higher value of the separation coefficient indicates a negligible overlapping between two consecutive wave packets. A separation coefficient equal to zero indicates a complete overlapping between the arrivals of a Lamb-like mode propagating along two consecutive helical paths. This

overlapping may lead to ambiguity in the tomography image reconstruction algorithm, due to the fact that damage could be located along either of these two helical paths.

Two notable configurations lead to $\kappa_{h,h-1} = 0$. The first is for $B = 0$ (i.e., for a transducer pair on the same meridional line, see Fig. 4). The second is for $B = \pi D / 2$ (i.e, for a transducer pair on two opposite meridional lines, see Fig. 4).

It should be noted that the separation coefficient decreases as the distance L increases (see Fig. 4). On the contrary, the separation coefficient increases as the diameter of the cylinder D increases. The proposed method is therefore well suited to large-diameter cylindrical structures. Incidentally, these types of structures also allow for the greatest accuracy in the assumption that the curved structure can be approximated by a plate waveguide. In comparing a small to a large diameter cylinder, a pair of transducers could be placed farther apart on the larger diameter cylinder in order to have a negligible overlapping between wave packets. Thus, a less dense array of transducers would be needed to monitor the cylinder with the larger diameter. In practice, however, increasing the length L in the large diameter cylinder will increase the length of all helical paths, which may cause attenuation to become a concern. Also, the spatial image resolution may be compromised, since a larger area between two transducers needs to be covered with a smaller ray density. This problem can be solved by using more helical paths.

2.2.3. Wave velocity

Up to this point the analysis has been restricted to only one Lamb-like wave mode propagating along multiple helical paths. However, more than one wave mode can propagate along a single helical path. To fully exploit the benefits of Lamb wave imaging, different modes should be automatically identified in a received signal, in order to extract the feature(s) of interest for the reconstruction algorithm [10]. Having multiple helical paths, however, makes this task very difficult. Furthermore, the dispersive behavior of Lamb waves, which causes their amplitude to spread out in the time domain, may cause overlapping between different arrivals. In general, this problem is more pronounced for higher-order (longer) helical paths.

Consider, for example, the first order helical path (i.e., the shortest path) between a transducer pair. For a given excitation frequency, the minimum time difference between the two fundamental Lamb-like modes A_0 and S_0 in a recorded waveform can be calculated as:

$$\Delta t_{Min}^{(S_0,A_0)} = \frac{l_1}{V_g^{(A_0)}} - \frac{l_1}{V_g^{(S_0)}} \tag{6}$$

At the appropriate frequency range and transducer placement, S_0 wave packets of the first few helical orders do not interfere with A_0 arrivals. This is due to fact that the group velocity of the S_0 mode is sufficiently larger than the A_0 mode at such frequencies. Fig. 5 shows the phase and group velocity dispersion curves for a 2.1 mm thickness steel pipe with 152 mm diameter. The excitation frequency should be selected within the shaded region for the following reasons: 1) GUWs in a curved shell can be approximated by Lamb waves [7]; 2) Only the two fundamental Lamb wave modes (i.e., A_0 and S_0) can propagate, and 3) The group velocities of A_0 and S_0 are nearly constant (i.e., the modes have low dispersivity), but the phase velocity of each is still dispersive enough to render it sensitive to thickness reduction [1] (see Fig. 5). Other advantages of using the constant group velocity (CGV) operation point of the A_0 mode were discussed by Nagy, et al. [1].

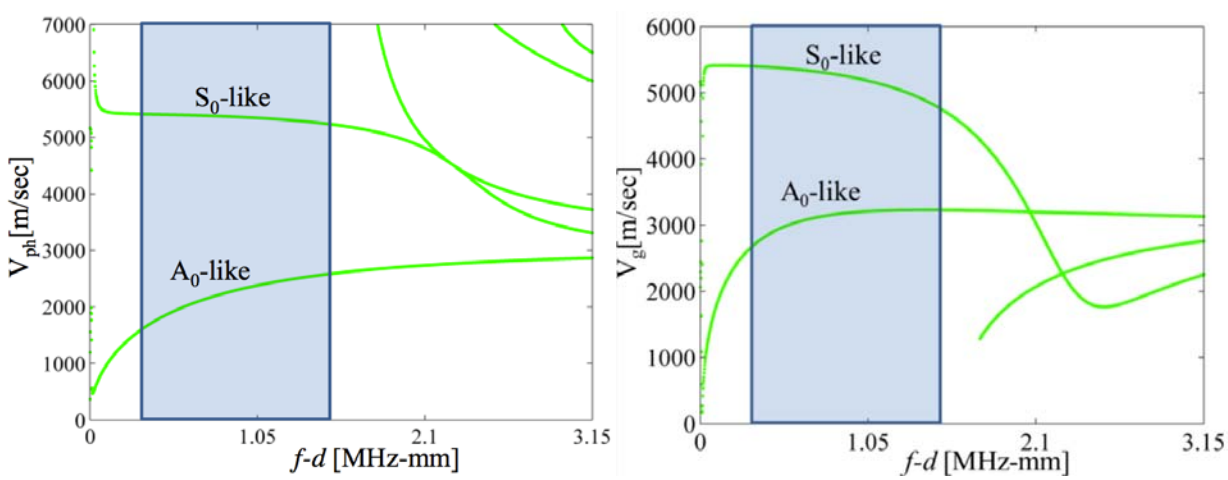

FIG. 5 Phase (left) and group (right) velocity across the frequency-thickness product. The shaded area shows the range of low dispersivity in the A_0 and S_0 mode group velocity.

2.2.4. Probabilistic reconstruction algorithm

In the past few years, several efforts have been made to combine Lamb waves and imaging algorithms for detecting and locating damage in complex structures [11]–[15]. In Lamb wave based imaging, the choice of the algorithm is crucial. Here, a modified probabilistic reconstruction algorithm (MPRA) is used in order to account for the contribution of different helical orders. The MPRA has many practical advantages, including flexibility in array geometry selection and, most importantly, it enables a reconstruction to be performed with both high quality and speed [11].

The MPRA spatially distributes and probabilistically accumulates differential features in an elliptical pattern. This method uses prerecorded baseline signals, measured while the structure is in a pristine state (i.e., damage free). Differential signals (i.e., subtraction of baseline signals from subsequently measured signals) are used to isolate the effects of damage introduced into the structure between the two measurements. Then, damage sensitive features $A_{kh}^{(m)}$ are extracted from the differential signals of N_h helical orders measured by N independent pairs of transducers. As a result, the number of paths that can be inspected significantly increases from N to $N \times N_h$ [1], [2]. The key idea behind the proposed approach is that the damage most significantly affects the helical paths that cross the damaged area. In this case, the definition of damage is a reduction in thickness, which simulates mass loss due to corrosion.

Depending on both the operational frequency of a Lamb wave and its dispersive behavior, phase and/or group velocity changes may occur due to the interaction of damage with the propagating wave. One of the other major changes that the ultrasonic field undergoes during propagation through different damage areas is its attenuation. Apart from material absorption, leakage, and scattering, which are the main causes of attenuation, there are two other phenomena, reflection and refraction, that are also responsible for the local attenuation of the ultrasonic signal in this context.

The damage feature introduced here is based on subtraction of the baseline and damaged signals. It is sensitive to both attenuation, due to any interaction of the wave with damage, and phase/group velocity changes due to thickness reduction. In addition, the statistical nature of the multiple helical

paths of multiple sensor pairs can enhance the sensitivity of the approach to damage to some extent [1].

The proposed MPRA algorithm can be formulated as:

$$P(x,y)=\sum_{k=1}^{N}\sum_{h=1}^{N_h}p_{kh}(x,y)=\eta\sum_{k=1}^{N}\sum_{h=1}^{N_h}A_{kh}^{(m)}\frac{\gamma_h-R_{kh}(x,y)}{\gamma_h-1} \tag{7}$$

where $P(x,y)$ is the estimation of the defect probability at the location (x,y) in the unwrapped configuration within the reconstruction region, and $p_{kh}(x,y)$ is the estimation from the k-th transducer pair and h-th helical order. N is the total number of independent transmitting and receiving pairs in a network of n_s transducers; this number can be calculated as $n_s(n_s-1)/2$. N_h is the maximum helical order used in the imaging algorithm. η is a probability scaling factor used to make the maximum probability equal to unity. γ is a scaling parameter which controls the size of the effective elliptical distribution area, where $\gamma > 1$. If γ is too small, then artifacts are introduced. However, if γ is too large, the resolution quality is sacrificed. Since a large value for γ may result in unwanted overlap of elliptical areas for the high helical orders in this research, a definition of γ as an inverse function of helical order h is proposed:

$$\gamma_h=1+\frac{\nu}{h} \tag{8}$$

The value of ν is a constant, which is determined by trial-and-error and set to $\nu = 0.025$ in this work. For the k-th pair and h-th helical order, R_{kh} can be calculated in the unwrapped representation as:

$$R_{kh}(x,y)=\frac{\sqrt{\left(x-x_{1k}\right)^2+\left(y-y_{1k}\right)^2}+\sqrt{\left(x-x_{2kh}\right)^2+\left(y-y_{2kh}\right)^2}}{\sqrt{\left(x_{1k}-x_{2kh}\right)^2+\left(y_{1k}-y_{2kh}\right)^2}} \tag{9}$$

where $\left(x_{1k},y_{1k}\right)$ and $\left(x_{2kh},y_{2kh}\right)$ are the transmitter and virtual receiver coordinates, respectively.

The contours of the distribution estimations are a set of ellipses with the two focal points being the transmitting and the virtual receiver for each pair, e.g., there are *h* ellipses for each pair of transducers. A set of helical waves of transmitting/receiving pair signals will be affected by the defect, while others will be less affected. As a result, in the defect distribution probability image, the pixel where the defect is located will have a larger probability others. The reconstruction of the final image is the accumulation and transformation of the constructed image from the artificial plates in the unwrapped coordinate system to the single unwrapped plate. In Eq. (7) the root mean square (RMS) of the differential signals are used as a damage-sensitive feature, that is:

$$A_{kh}^{(m)}=\frac{\int_{t_h^{(m)}}^{t_h^{(m)}+\Delta\tau}\left[S_k(t)-H_k(t)\right]^2dt}{\int_{t_h^{(m)}}^{t_h+\Delta\tau}\left[S_k(t)\right]^2dt} \tag{10}$$

where $S_k(t)$ and $H_k(t)$ are the baseline and the current signal, respectively. $\Delta\tau$ is the excitation pulse duration. $t_h^{(m)}$ is the arrival time of *h*-th helical order packets of the *m*-th Lamb wave mode, and can be estimated from Eq. (2). Therefore, N_h features will be extracted from each independent pair of transducers.

2.2.5. Experimental Results

Experiments were carried out using a 3 m long steel pipe with a 152.4 mm diameter and 2.1 mm thickness to validate the proposed algorithm of mapping thickness loss. Six piezoelectric

transducer (PZT) disks (see Fig. 6) were permanently attached to the surface of the pipe using a Loctite instant adhesive. A 2 m middle section of the pipe was instrumented, in order to avoid reflections from the pipe ends. The specimen was gridded longitudinally and circumferentially at 40 mm and 1/8th increments, respectively, as shown in Fig. 6. Each PZT sensor was connected to a 40 dB preamplifier. Signal generation and data acquisition were achieved with a National Instruments (NI), modular PXI 1042 unit. This unit included an arbitrary waveform generator card (PXI 5411) and one 20 MS/s 12-bit multi-channel digitizers (PXI 5105). In addition, a high voltage amplifier was used to amplify the excitation to the ultrasonic transmitters. A 5-cycle ultrasonic toneburst with a center frequency of 700 kHz (1.47 MHz-mm based on the pipe thickness) was used as an excitation. This frequency was selected to meet the requirements described earlier; that is, below the first cut-off frequency (1.6 MHz-mm), and in a frequency range in which A_0 has low dispersivity (see Fig. 5).

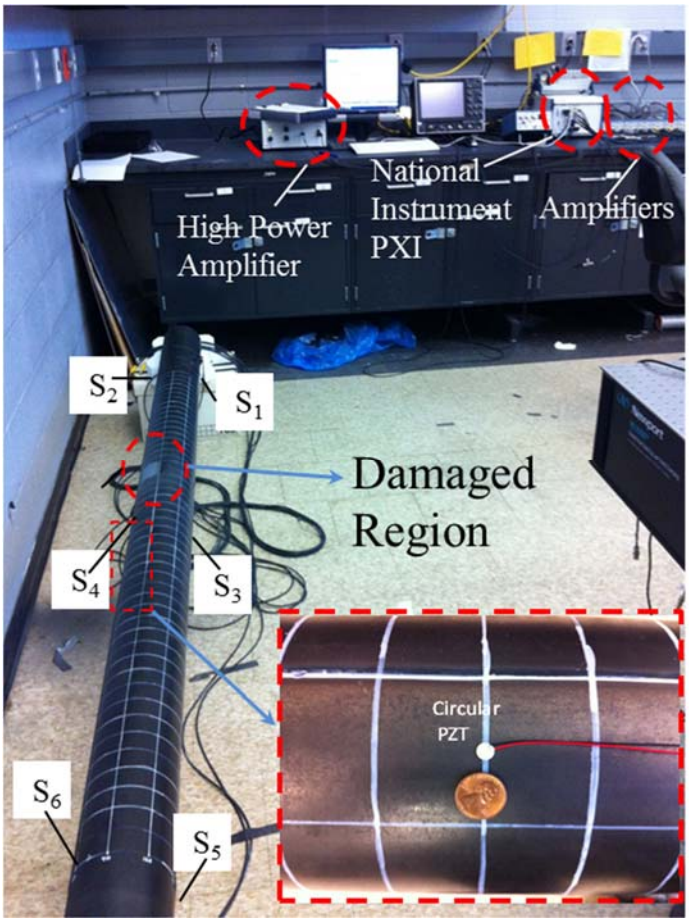

FIG. 6 Steel pipe experimental setup and data acquisition system. PZT sensors are labeled $S_{1,2,\ldots,6}$.

Fig. 6 shows the overall experimental setup. Three thickness recesses simulating corrosion were engineered by machine cutting. The in-plane dimensions of the defects were $30\ \text{mm} \times 40\ \text{mm}$, $30\ \text{mm} \times 80\ \text{mm}$, and $60\ \text{mm} \times 80\ \text{mm}$, with depth equal to 40% of the wall thickness of the pipe, as shown in Fig. 7. It should be noted that the wavelength for the A_0 mode at the excitation frequency was much smaller (λ = 3.7 mm), than the damage size. Therefore, the A_0 mode was sensitive enough to the simulated damage sizes.

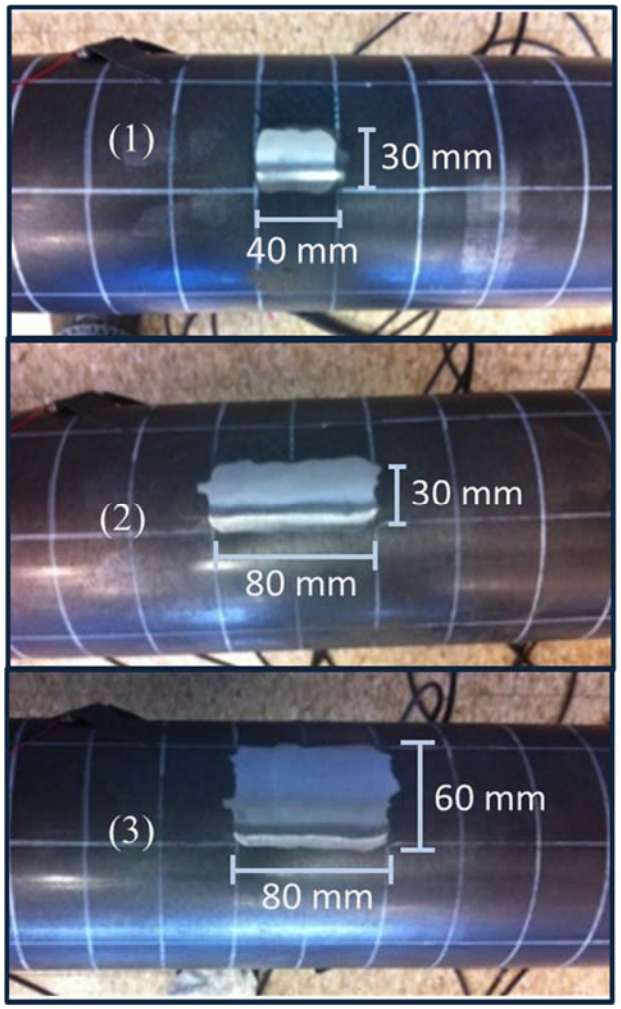

FIG. 7 Three cases of simulated corrosion (thickness reduction) in the steel pipe of Fig. 6.

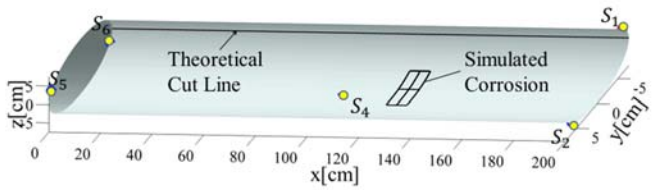

FIG. 8 Schematic view of the sensor network and simulated corrosion.

Trans./Rec. Pair #	Trans. #	Rec. #
1	1	3
2	1	4
3	1	5
4	1	6
5	2	3
6	2	4
7	2	5
8	2	6
9	3	5
10	3	6
11	4	5
12	4	6

TABLE I. Listing of unambiguous sensor pairs.

Fig. 8 shows a schematic view of the experimental setup; including the transducer layout and simulated damaged region, in both a 3D view and in the unwrapped equivalent plate. The six transducers were divided in three groups, (S1,S2), (S3,S4), and (S5,S6). The transducer layout was designed according to the guidelines suggested earlier and, as such, no pairs of transducers were placed on the same meridional line of the test specimen. For each group, two transducers were placed symmetrically with respect to the center axis of the pipe. Symmetric placement of transducers guarantees a uniform density distribution of helical paths and thus better quality images [13]. It should be noted that this configuration may lead to ambiguous results. To remove this ambiguity, transducers within the same group were not included in the MHUI algorithm. The total number of unambiguous independent transducers can be calculated as:

$$N = \frac{(n_s - 1)n_s}{2} - \left(\#\text{ of ambiguous transducer pairs}\right) \tag{11}$$

where n_s is the total number of transducers used. As per Eq. (11), the number of unambiguous independent transducers pairs in the network was $N = 12$; these pairs are listed in Table I. The maximum number of helical orders N_h used in the proposed imaging algorithm was set to nine.

For illustrative purpose, the first six helical paths between transducers 1 and 3 on the unwrapped plate are shown in Fig. 9. The separation coefficients between transducer 1 and the other five transducers for the first nine helical orders are listed in Table II (this table is associated with transmitter/receiver pairs #1-4). In this table, except for transducers of in the same group, the separation coefficients related to each pair of transducers is non-zero (unambiguous) and thus the signal packets related to a single Lamb wave propagating along these helical paths can be used as an input to the image reconstruction algorithm. From a damage-free state, baseline signals were recorded, one for each transducer pair.

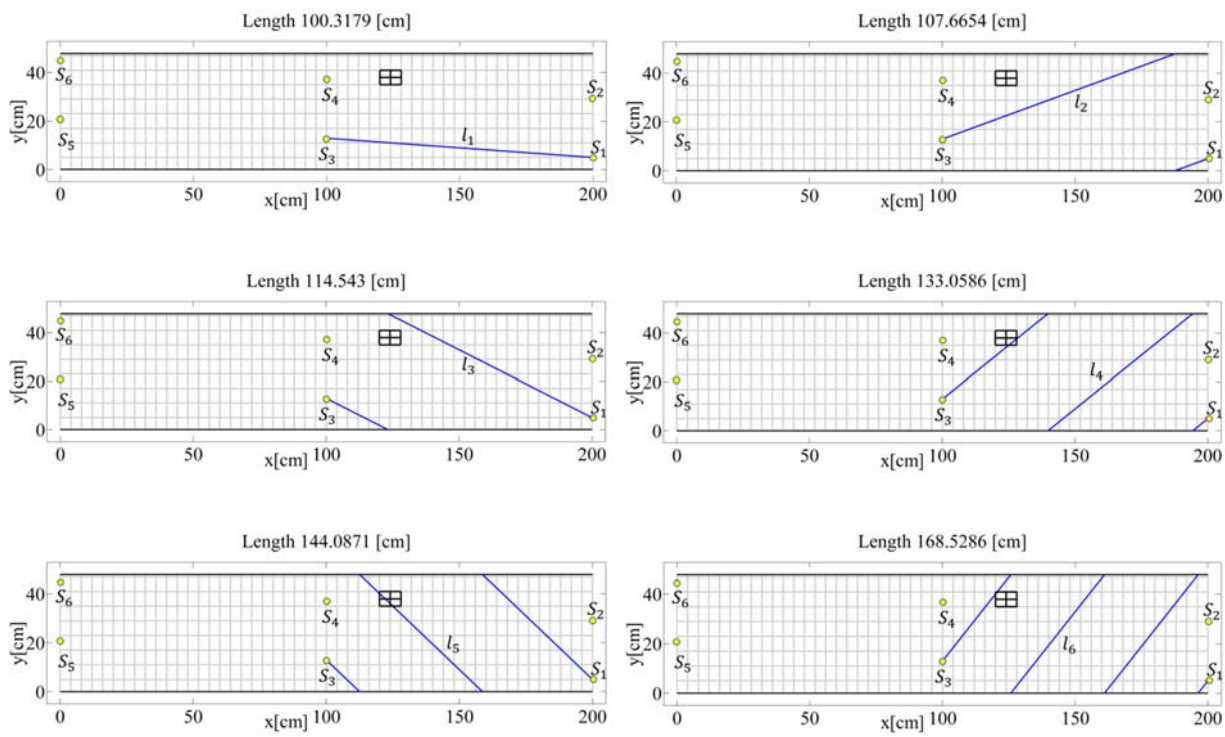

FIG. 9 Schematic of the first six helical paths between sensors S1 and S3.

S	2	3	4	5	6
B[mm]	$\pi D/2$	$\pi D/6$	$\pi D/3$	$\pi D/3$	$\pi D/6$
L[mm]	0	1000	1000	2000	2000
β	NA	0.08	0.16	0.08	0.04
δ	0	0.15	0.15	0.076	0.076
$\kappa_{2,1}$	0	0.073	0.037	0.0095	0.019
$\kappa_{3,2}$	0	0.068	0.136	0.0370	0.019
$\kappa_{4,3}$	0	0.185	0.093	0.0270	0.054
$\kappa_{5,4}$	0	0.110	0.220	0.0688	0.034
$\kappa_{6,5}$	0	0.244	0.122	0.0410	0.082
$\kappa_{7,6}$	0	0.130	0.262	0.0930	0.046
$\kappa_{8,7}$	0	0.273	0.137	0.0512	0.102
$\kappa_{9,8}$	0	0.141	0.283	0.1102	0.055

TABLE II. Separation coefficients between sensor S1 and all others. Values for the first nine helical orders are listed.

In Fig. 10 the signals measured in the undamaged (baseline) and damaged conditions are overlain; the first six helical waves for the fundamental modes (S_0, A_0) are also indicated. Fig. 11 shows the differential signal (i.e., subtraction of baseline signals from current signals) and the gated signal used in Eq. (10). It can be noted that, as expected, the A_0 mode appears more sensitive to damage (thickness loss) than the S_0 mode. Therefore, the A_0 mode can be considered an ideal candidate to identify the type of defects simulated in this study. It is noteworthy that the differential signal relative to the helical orders that pass through the damaged region increases (see Fig. 11, helical orders 4, 5, and 6).

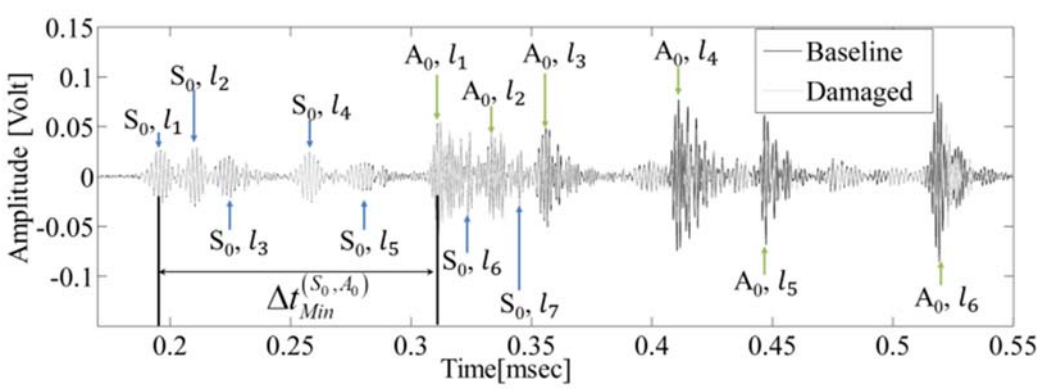

FIG. 10 Received signals for the baseline and damaged case.

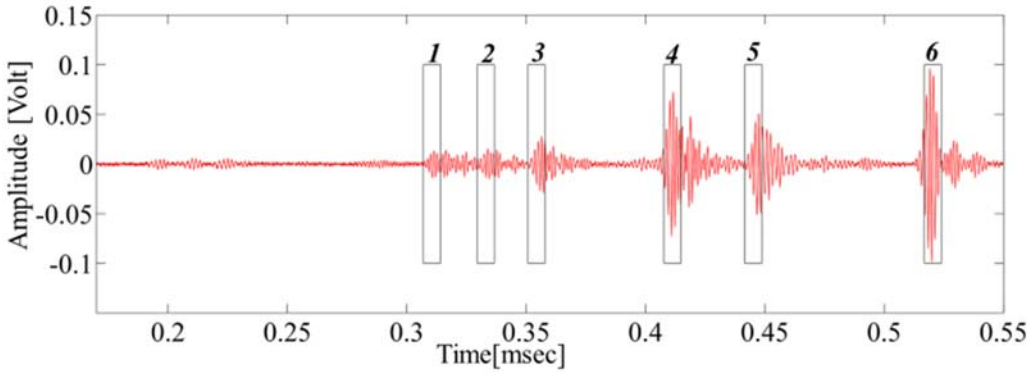

FIG. 11 Differential signal for the baseline and damaged states shown in Fig. 10.

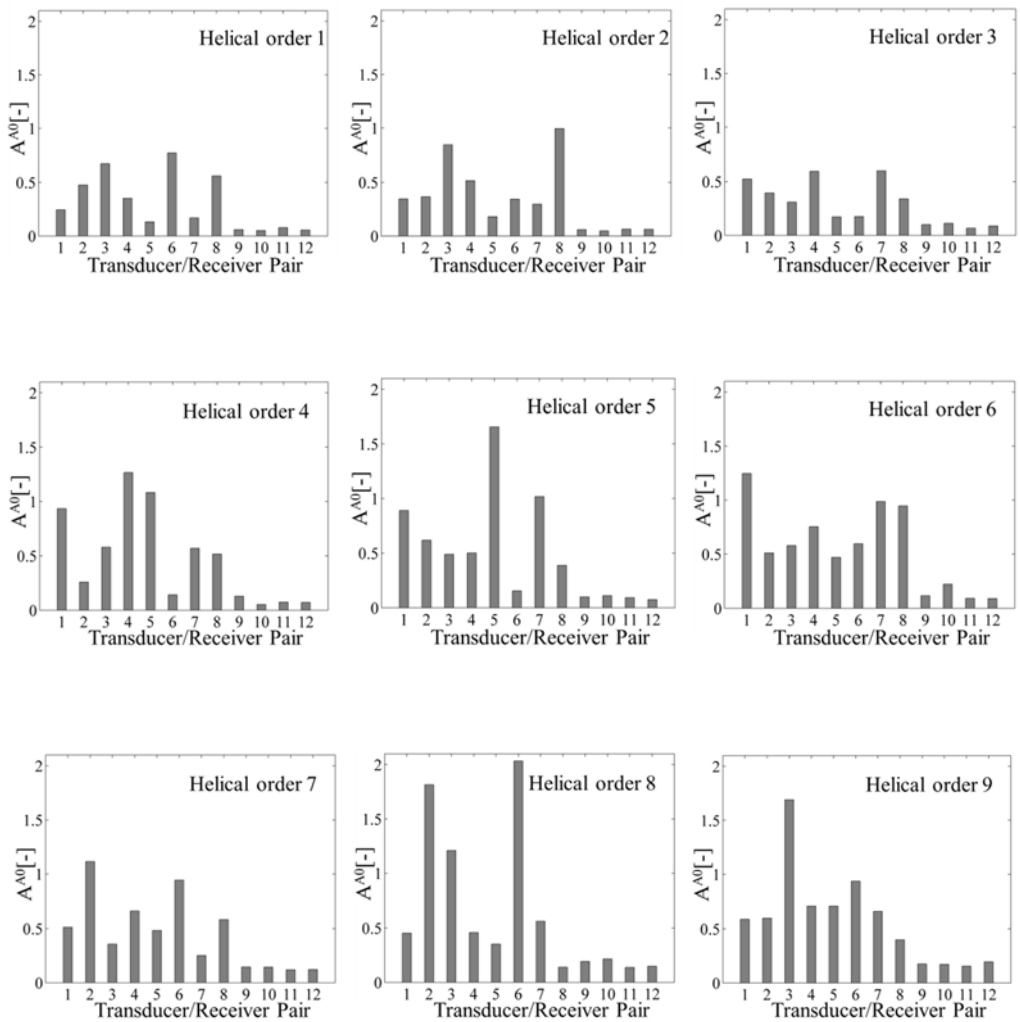

FIG. 12 Damage sensitive feature values for the 12 sensor pair for the first nine helical orders.

Fig. 12 shows the damage-sensitive feature $A_{kh}^{(m)}$ for the twelve transducers pairs and nine helical orders for the defect case #3. Small values of $A_{kh}^{(m)}$ indicate that the related helical path was not affected by the defect while, on the contrary, large values indicate the presence of damage along the associated helical path.

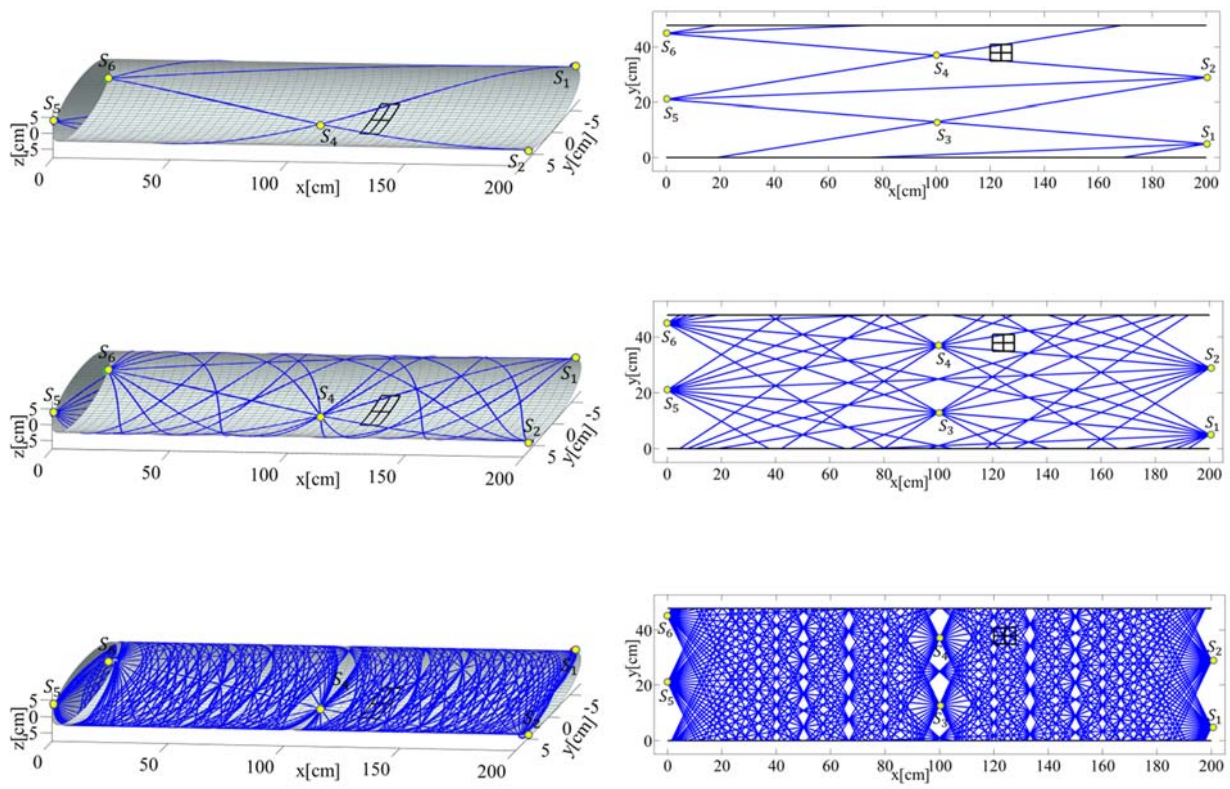

FIG. 13 1st, 3rd, and 9th helical paths between all sensor pairs. Left: Cylinder. Right: Unwrapped representation.

Fig. 13 shows the first, third and ninth order helical paths between all twelve transducer pairs. It should be observed that the rays in the first and third order helical paths do not intersect the damage region so that, as will be shown, the damage cannot be reliably detected in these two cases. Furthermore, the resolution/ray density can be increased by simply increasing the maximum number of helical order N_h. Therefore, the resolution of the image can be improved by considering a large number of rays passing through the damaged area, without the requirement of increasing the number of transducers. It is worth noting that this resolution is artificial, and in practice cannot be infinity, due to limitations in measurement and wave propagation. Among these limitations, the

maximum signal length recording capability of the data acquisition system and attenuation are more important for very high helical order consideration. Furthermore, since in the proposed MHUI the higher order helical paths cross the damaged area at different angles, smearing effects will be reduced [4].

Fig. 14 shows the results of the image reconstruction obtained for the defect case I when the first, third and ninth helical orders related to the A_0 mode were used. It can be seen that the quality of both the image and damage detection improve as the number of helical orders considered in the algorithm increases. It is noteworthy that images exhibit minimal artifacts by using only six transducers.

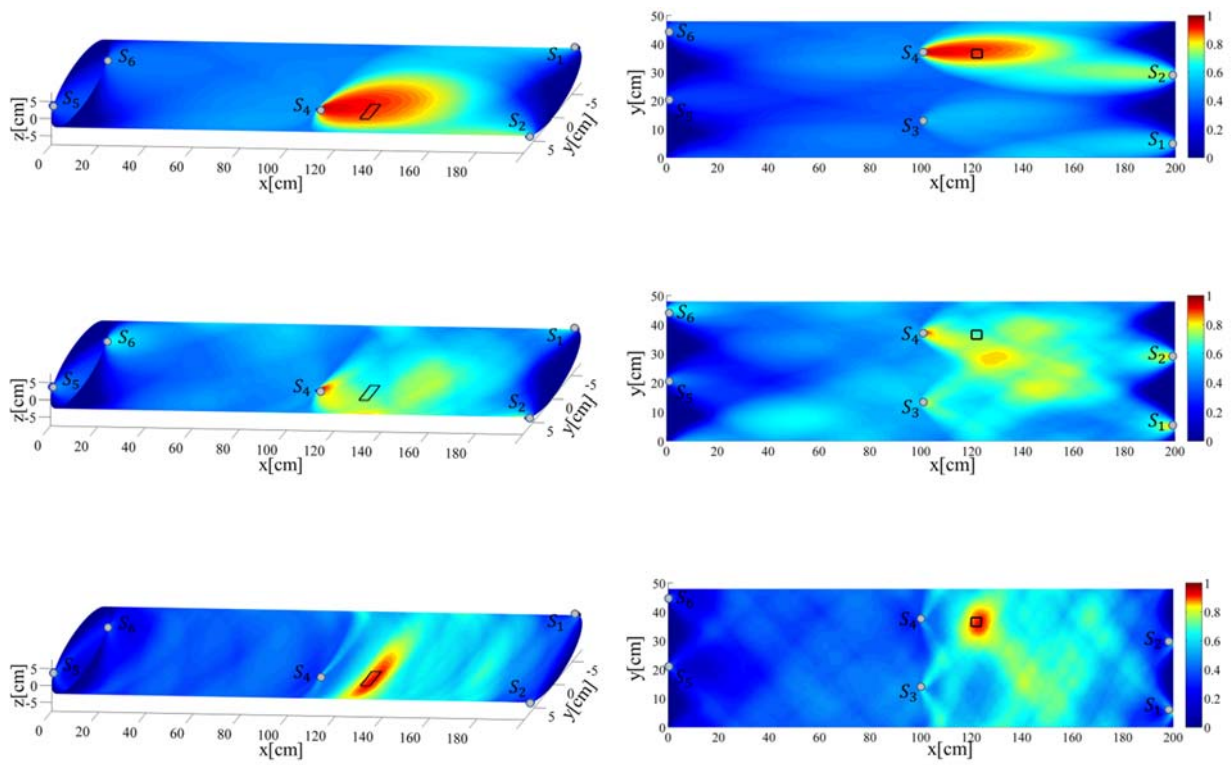

FIG. 14 Image reconstruction of thickness loss due to damage case I. Left: cylindrical structure. Right: unwrapped representation of the cylinder.

The present image reconstruction algorithm is not based on the validity of the ray theory in which the ray paths/directions are not influenced by the inhomogeneities in the medium (for more details the reader may refer to P. Belanger and P. Cawley [16]). The relative sensitivity of the extracted

damage feature to thickness changes is very important. Operational frequency can change the wavelength and, as a result, change this relative sensitivity due to change in wave interaction with damage. In order to evaluate the validity of our assumption and the effectiveness of the MHUI at different frequencies/wavelengths, four different operational frequencies listed in the Table III are considered.

Frequency (MHz-mm)	A_0 Wavelength(mm)	Max Damage size to wavelength ratio
1.47	3.6	40/3.6=10.8
0.63	6.8	40/6.8=5.88
0.42	8.9	40/8.9=4.5
0.21	13.4	40/13.4=3

TABLE III. Operational frequencies considered in the MHUI algorithm for the A_0 mode.

Fig. 15 shows the 5th helical order of twelve independent transmitter/receiver pairs listed in Table I. Among these 5th order helical paths, ones that are related to the first, fifth and seventh pairs cross through the first damage stage zone. In Fig. 15 the solid red, dashed black and dashed dot green lines correspond to the first, fifth and seventh transmitter/receiver pairs respectively. Fig. 16 shows the damage-sensitive features $A_{kh}^{(m)}$ for the twelve transducers pairs and the fifth helical orders for the defect case I at the four operational frequencies listed in Table III. Although reducing the damage size to wavelength ratio reduces the value of the damage feature, the damage-sensitive features related to the three paths that go the defect area are relatively more than that of other paths. This contrast in the damage-sensitive feature indicates that the assumption on which the algorithm is based is valid. The contrast in the damage-sensitive feature, however, reduces as the excitation frequency reduces. This happens because of inaccuracy in feature extraction due to overlapping in signal packets of consecutive helical paths. Two reasons cause this inaccuracy in feature extraction: 1) The dispersive group velocity of A_0 at this frequency causes overlapping in the signal packets and violates the constant wave velocity assumption used in the feature extraction, and 2) The low frequency causes large time duration (the number of excitation's cycle is constant), so that the signal packets are more likely to interfere with each other. Despite the fact that the current method is not based on the validity of the ray theory, diffraction might be another reason for

reducing the contrast, as a result of reduction in damage size to wavelength ratio and should be considered if the damage size is much smaller than wavelength.

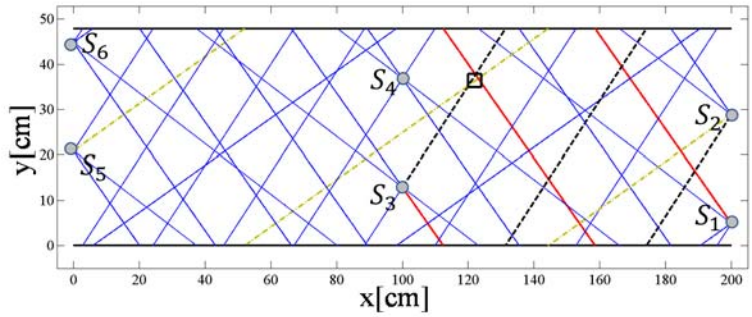

FIG. 15 Fifth order helical paths for the 12 sensor pairs listed in Table I.

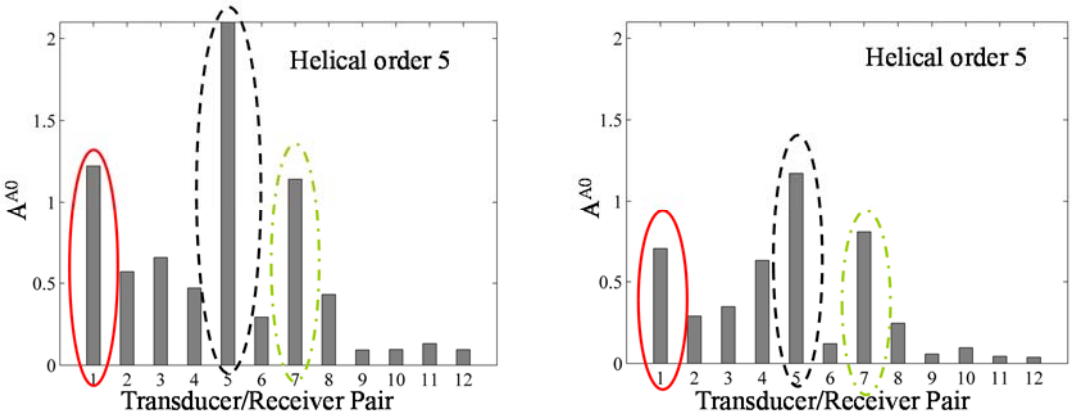

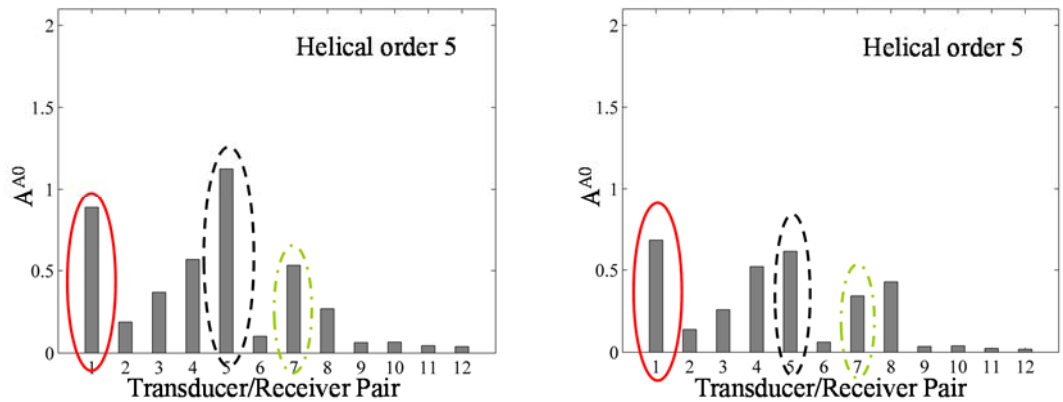

FIG. 16 Damage sensitive features for the 12 sensor pairs at the four operational frequencies listed in Table III.

The image reconstruction results obtained using nine helical paths for the defect case II and III for the 700 kHz operational frequency are shown in Fig. 17. Up to this point, no attempt was made to quantify the extent of the thickness reduction. However, a quantitative measurement of the thinning depth can be obtained by customizing the MHUI algorithm. Furthermore, the image reconstruction can be enhanced by modifying Eq. (7) to include additional Lamb wave modes, frequencies, and helical orders, as follows:

$$\begin{aligned} P(x,y) &= \sum_{i=1}^{N_f}\sum_{m=1}^{N_m}\sum_{k=1}^{N}\sum_{h=1}^{N_h} p_{ikh}^{(m)}(x,y) \\ &= \eta\sum_{i=1}^{N_f}\sum_{m=1}^{N_m}\sum_{k=1}^{N}\sum_{h=1}^{N_h} A_{ikh}^{(m)}\frac{\gamma - R_{kh}(x,y)}{\gamma - 1} \end{aligned} \tag{12}$$

where N_f and N_m are the number of operational frequencies and Lamb modes used in the image reconstruction.

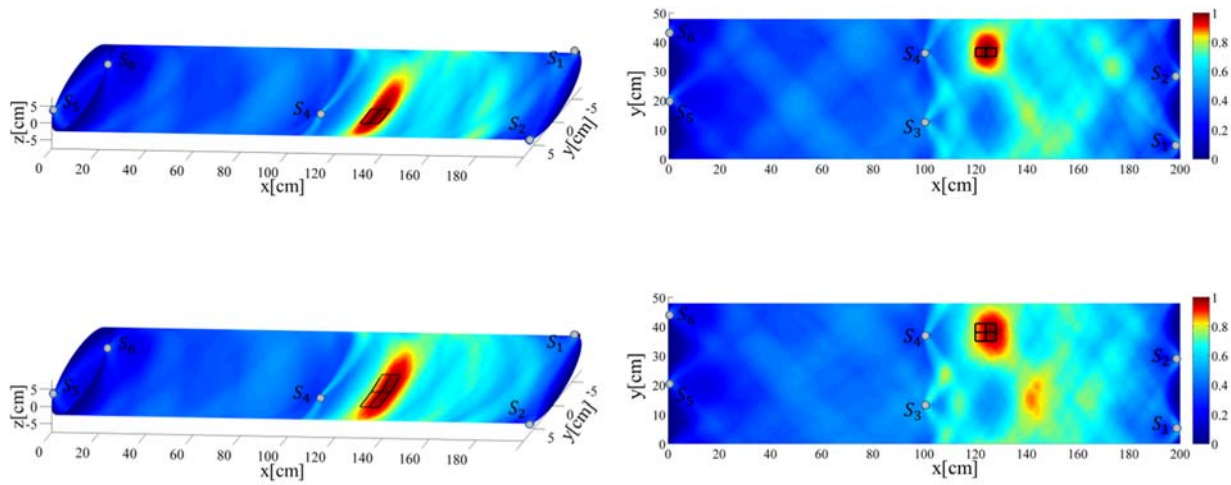

FIG. 17 Image reconstructions of thickness loss for damage cases II and III. Left: cylindrical structure. Right: unwrapped representation of the cylinder.

2.3. Quantitative Thickness Loss Evaluation

2.3.1. Corrosion patch quantification

Consider a corrosion patch in the unwrapped coordinate system, as shown in Fig. 18. Fig. 18 also shows the corresponding reconstructed image intensity $I(x, y)$ obtained using the MHUI algorithm. The method proposed here is to estimate the boundary of the corrosion patch $\Gamma(x, y)$, along with its remaining thickness. One of the major assumptions associated with this method is that ray theory is valid. For this assumption to be satisfied, the characteristic size of the defect must be larger than the wavelength (λ), and larger than the width (L_f) of the first Fresnel zone, which can be approximated in the middle of the ray path as [16]–[18]:

$$L_f(\frac{l}{2}) = \sqrt{l\lambda} \tag{13}$$

where l is the length of the ray path between a pair of transducers. Two additional assumptions are made also made at this point: 1) Scattering effects are negligible, and 2) Thickness changes are

uniform within the area of corrosion. For simplicity, it is assumed that only a single defect is present.

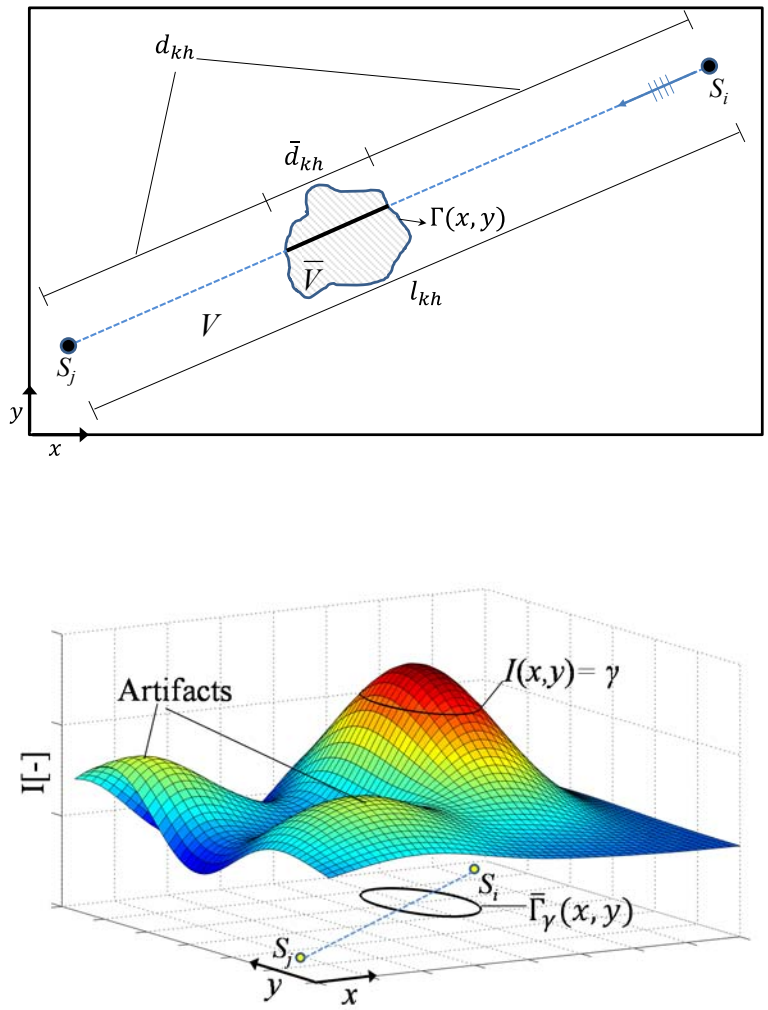

FIG. 18 Schematic of a corrosion patch between a pair of sensors and the corresponding image intensity.

Thickness mapping results using time-of-flight straight ray tomography algorithms largely depend on the selection of the operational frequency. This frequency should be selected below the first cut-off frequency to ensure that higher wave modes do not contaminate the signals, and also within a frequency range where the dispersion of the two fundamental modes (A_0 and S_0) is significant. A review of the operational frequency selection was presented in [19]. In that paper, it was shown that if the operational frequency is selected below the first cut-off frequency, there are two likely regions of operation for A_0 and S_0. These two ranges in frequency are shown in Fig. 19 and

highlighted by wide black lines. The A_0 mode is more sensitive to thickness changes, because of the steep gradient of the dispersion curve below fd = 1 MHz·mm. In this frequency range, a small change in thickness results in a large change in group velocity, resulting in a higher sensitivity to thickness loss. For this and other reasons, we restrict our analysis to the A_0 mode.

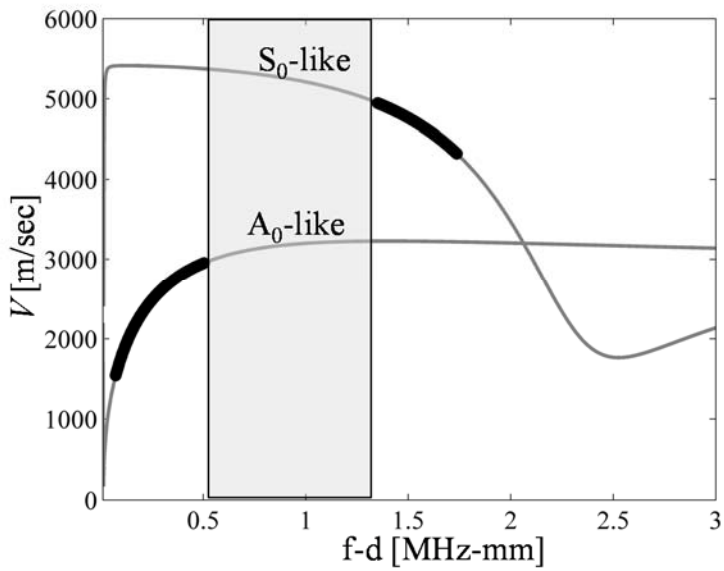

FIG. 19 Group velocity dispersion curves for the A_0 and S_0 wave modes. Shaded areas indicate low dispersivity. Thickened lines indicate high dispersivity.

Due to the dispersive nature of the A_0 mode in the considered frequency range, the wave velocity changes as it propagates in the corrosion patch. If the boundary $\Gamma(x, y)$ of the corrosion patch can be approximated with one unique contour of the image, defined as $I(x, y) = \gamma$, then the problem of finding $\Gamma(x, y)$ reduces to estimating the counter level γ, whose boundary is $\overline{\Gamma}_\gamma(x, y)$, as shown in Fig. 18. To estimate the remnant wall thickness, the dispersive nature of Lamb waves travelling through the pipe is exploited to convert the thickness changes into wave velocity variations, providing a mechanism to determine thickness from a velocity reconstruction $\overline{V}$ in the corrosion area.

Consider a transmitting (S_i) and receiving (S_j) sensor, associated with the k-th transmitter/receiver pair, with a corroded area located along the path, as shown in Fig. 18. The total travel time T_{kh}

from the transmitter S_i to the receiver S_j through the h-th helical path is defined in Eq. (2) (V is the wave velocity in the pristine structure). Due to the lower thickness in the corrosion area, the wave velocity in the will change to $\overline{V}$ in this section of the structure. The travel time between the two sensors will then change accordingly as:

$$\overline{T}_{kh} = \frac{\overline{d}_{kh}}{\overline{V}} + \frac{d_{kh}}{V} \tag{14}$$

where $\overline{d}_{kh}$ and d_{kh} are the portions of the helical path inside and outside of the corrosion patch, respectively (see Fig. 18). Having the image information $I(x, y)$, and based on the assumption that $\Gamma(x, y)$ can be approximated by $\overline{\Gamma}_{\gamma}(x, y)$, the $\overline{d}_{kh}$ and d_{kh} lengths can be calculated for different contour levels γ. The time difference in the total travel time before and after corrosion can be defined as:

$$\Delta T_{kh} = \overline{T}_{kh} - T_{kh} \tag{15}$$

It should be noted that since the A_0 mode is used, a reduction in wave velocity V in the presence of corrosion is expected (see Fig. 19), and thus an increase in the total travel time T_{kh} (i.e., ΔT_{kh} is positive).

The total helical path length l_{kh} between the two sensors is equal to:

$$l_{kh} = d_{kh} + \overline{d}_{kh} \tag{16}$$

The time differences ΔT_{kh} can then be calculated for different contour level γ and wave velocity $\overline{V}$ as:

$$\Delta T_{hk} = \overline{d}_{kh}(\frac{1}{\overline{V}} - \frac{1}{V}) \tag{17}$$

The actual time differences $\overline{\overline{\Delta T}}_{kh}$ associated with h-th helical order of k-th transducers pair can be experimentally measured using received signals $S_k(t)$ and $H_k(t)$ from the pristine and damaged conditions, respectively. A common method to estimate the time of arrival difference is cross-correlating the gated signals ($S_k(t)$ and $H_k(t)$) and selecting the peak of the correlogram as the estimated time difference. The gated correlogram is:

$$z_{kh}(\tau) = \frac{1}{\Delta t}\int_{T_{kh}^{(m)}}^{T_{kh}^{(m)}+\Delta t} S_k(t)H_k(t+\tau)dt \tag{18}$$

where Δt is the excitation pulse duration and $T_{kh}^{(m)}$ is the arrival time of the mode under consideration. The time of arrival difference $\overline{\overline{\Delta T}}_{kh}$ can now be estimated as the value of τ that maximizes the correlogram $z_{kh}(\tau)$.

Having the measured time differences in Eq. (18) and their theoretical counterparts from Eq. (17), a weighted least-square minimization problem is proposed in order to estimate the contour level γ and wave velocity $\overline{V}$ as:

$$\min J(\gamma, \overline{V}) = \sum_{k=1}^{N}\sum_{h=1}^{N_h}(\Delta T_{kh} - \overline{\overline{\Delta T}}_{kh})^2 w_{kh}\delta_{\overline{\overline{\Delta T}}_{kh}>0} \tag{19}$$

where N is the number of independent transducer pairs, and N_h is the number of helical orders used in the image reconstruction. In Eq. (19) the w_{kh} is the damage index given in Eq. (10) and $\delta_{\overline{\overline{\Delta T}}_{kh}>0}$ is an indicator function defined as:

$$\delta_{\overline{\overline{\Delta T}}_{kh}>0} = \begin{cases} 1 & if \ \ \overline{\overline{\Delta T}}_{kh} > 0 \\ 0 & if \ \ \overline{\overline{\Delta T}}_{kh} \leq 0 \end{cases} \tag{20}$$

The indicator function eliminates the error components with positive time delay. The reason for this elimination is that, since the A_0 mode was used, a positive delay was expected for a loss in thickness. As discussed in [16], if the Fresnel zone is not much smaller than the damage size (the first condition of the straight ray theory) thickness loss may cause an increase in the wave velocity of A_0 (see Fig. 5 in [16]). The higher the helical order, the larger the helical path between a pair of transducers. Thus, according to Eq. (13), the value of the first Fresnel zone is larger for high helical orders. As a result, the first condition of the straight ray theory is not strictly met in the method proposed here. To overcome this issue, these error components were eliminated from the least-square objective function in Eq. (19). Furthermore, the weighting component w_{kh} was introduced to increase the weight/contribution of the helical paths with a higher damage index. The reason for this weighting is to increase the contribution of error components associated with the helical paths that are more likely to travel through the corrosion patch.

It is worth noting that the objective function in Eq. (19) is not in parametric form, so that a gradient based optimization method cannot be easily used. Several derivative free algorithms have been developed in the literature for minimizing the objective function of Eq. (19), such as Genetic Algorithms (GA) [20], Particle Swarm Optimization (PSO), and Mesh Grid Optimization (MGO) or coordinate search [21]. Here, a MGO algorithm was used, with 0.001 and 5 m/s increments for γ and $\overline{V}$ respectively. Therefore, the values of γ and $\overline{V}$ were estimated by evaluating the objective function in Eq. (19) at gridded parameters. The corresponding absolute minimum value represents the unknowns γ and $\overline{V}$. Overall, the proposed quantitative corrosion imaging approach

is shown in Fig. 20. It consists of two main stages. In the first stage, a qualitative image is reconstructed using the MHUI algorithm. In the second stage, quantitative information (i.e., location, area and thickness) are estimated by solving an optimization problem.

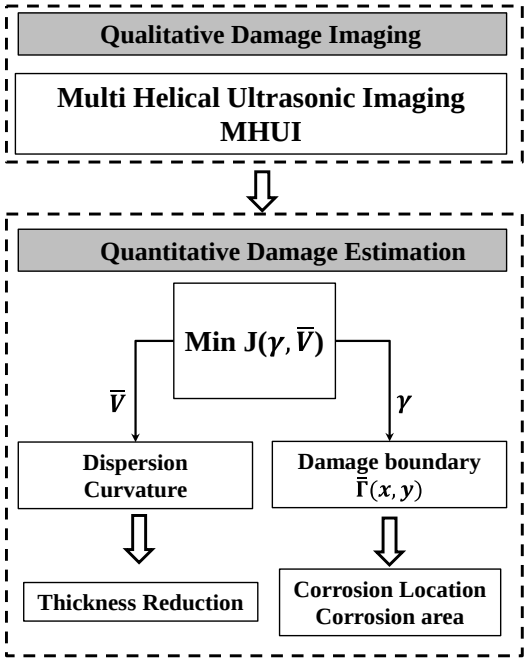

FIG. 20 Algorithm logic for the image reconstruction approach to estimating thickness loss.

2.3.2. Experimental results

The experimental results presented here are an extension of those presented earlier in the section on the mapping of thickness loss regions. The setup is thus the same, and that section may be referenced for more details. It should be noted that the wavelength for the A_0 mode at the excitation frequency in the second stage is much smaller, than the smallest damage size (i.e. 7.91<<30). This value satisfies the second condition of the straight ray theory. However, the wavelength, particularly in the quantitative stage, does not strictly satisfy the ray theory in which the damage size should be less than the first Fresnel zone in Eq. (13) of all helical paths. For example, the width of the first Fresnel zone of first helical order for transducer pairs 1-3 is 89 mm ($\sqrt{1003.1 \times 7.9} = 89 > 30$). The effect of this problem can be to some extent compensated by eliminating the error components with positive delay value in Eq. (19).

The image reconstruction results obtained using MHUI for the corrosion case I, II and III are shown in Fig. 21. These qualitative images will be used for quantifying the corrosion patch.

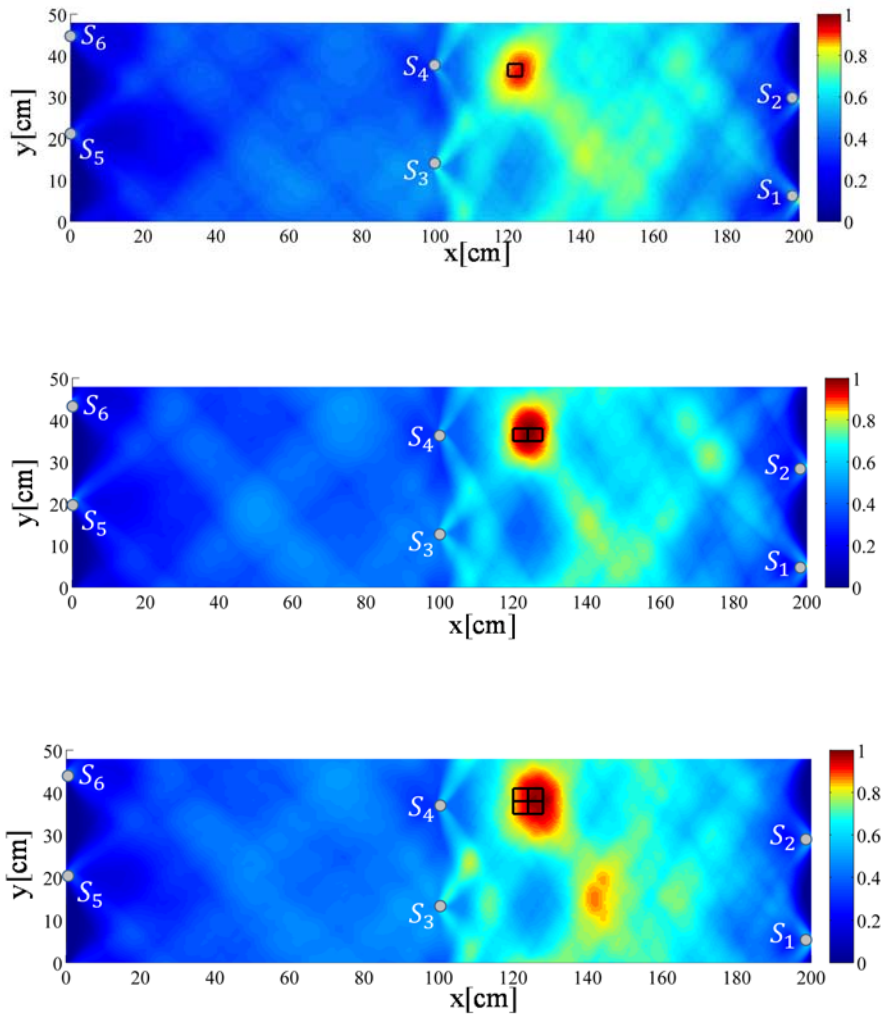

FIG. 21 Image reconstruction of thickness loss regions for damage cases I, II, and III.

Consider an image associated with the corrosion case I with image intensity $I(x,y)$ (see Fig. 21). A number of contours associated with different values of γ can be identified, as shown in Fig. 22. The projections of each contour line $\overline{\Gamma}_{\gamma}(x, y)$ in the unwrapped configuration is depicted in Fig. 22. It is worth noting the existence of several artifacts at the sensor locations. These artifacts occur due to the accumulation of several elliptical shapes with the focal points being at each sensor

location. This problem is solved in the image by smoothing the sensor area and eliminating the contour lines associated with these artifacts.

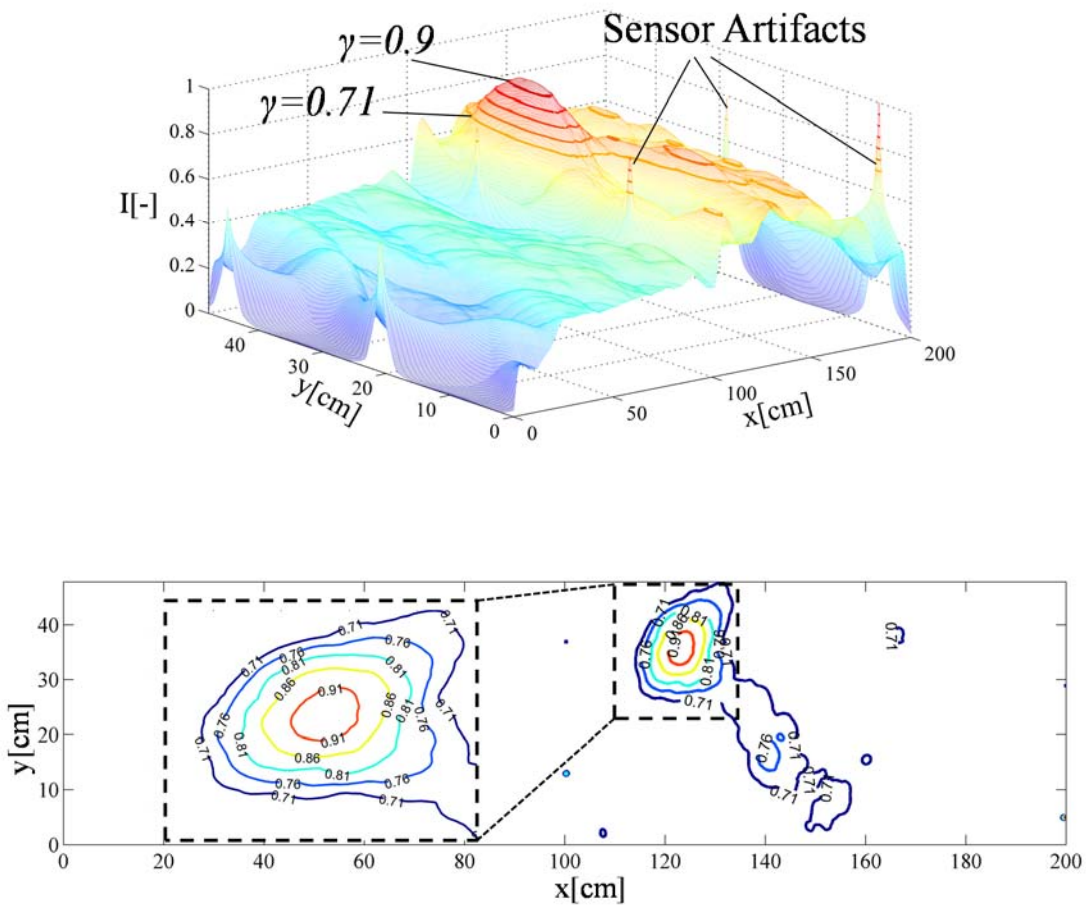

FIG. 22 Image intensity contour levels for damage case I.

Having $\overline{\Gamma}_{\gamma}(x,y)$ at a particular level and based on the geometry of the sensor network the portion of each helical path $\overline{d}_{kh}$ that goes inside contour $\overline{\Gamma}_{\gamma}(x,y)$ can be theoretically determined. For illustrative purpose, in Fig. 23 the $\overline{d}_{kh}$ are shown with bold gray lines inside the $\overline{\Gamma}_{0.71}(x,y)$. These values are used for calculating the objective function in Eq. (19) at gridded values of γ and group velocity $\overline{V}$ inside the corrosion patch. A surface plot of the logarithmic values of weighted least-square error in Eq. (19) for the corrosion case I is given in Fig. 24. It can be observed that the objective function is convex, and its minimum value is located at a contour level of $\gamma = 0.987$ and

a group velocity of 2785.8 m/s. The centroid and the area of $\overline{\Gamma}_{\gamma}(x, y)$ indicates the location and corrosion patch size, respectively. Furthermore, one can use the dispersion group velocity to find the remnant thickness associated with the estimated wave velocity $\overline{V}$ inside the corrosion patch. The estimated boundaries $\overline{\Gamma}_{\gamma}(x, y)$ of the three simulated corrosion patches are shown in Fig. 25. The contour levels γ, area, and the location associated with these boundaries and the thickness loss associated with the estimated wave velocity $\overline{V}$ in the corrosion patch are given in Tables II and III, respectively.

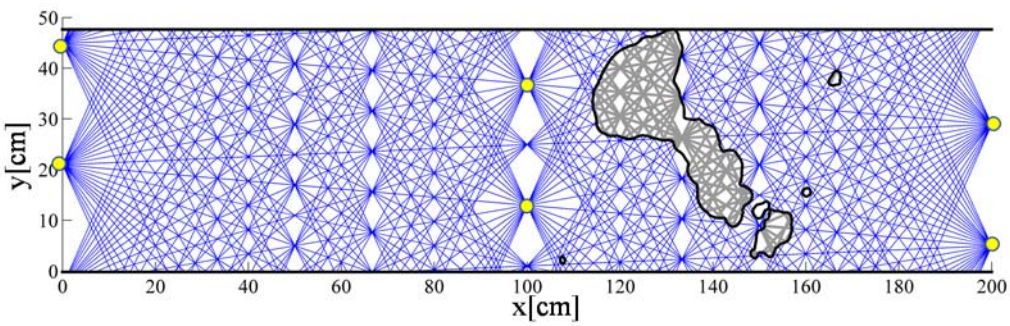

FIG. 23 Example of a contour level of γ = 0.71 for damage case I.

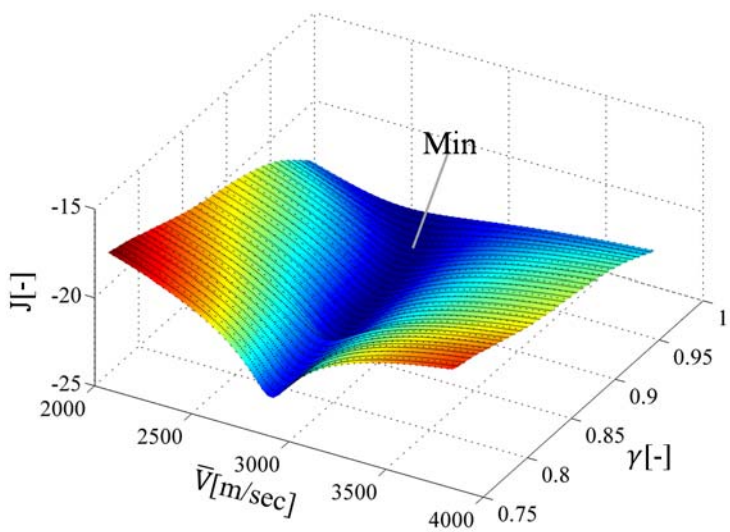

FIG. 24 Error in objective function on a logarithmic scale for different trial values of group velocity and γ.

Results show a reasonable agreement between the estimated and the actual value of the location. However, the corresponding areas are slightly overestimated for cases I and II. There are two possible causes of this error: 1) Since in general the direction of the higher order helical paths going through the damage area tend to be more vertical, the horizontal dimension of the corrosion patch cannot be accurately captured. Fig. 25 shows that the maximum error among the three corrosion cases is related to case II where the shape of the corrosion patch is elongated in the horizontal direction. 2) The violation of the ray theory condition related to the Fresnel zone. Although the characteristic size of the corrosion in all cases is comparable to the wavelength λ, for corrosion case I and II their size is smaller than the width of the Fresnel zone.

Corrosion Stage	I	II	III
γ	0.920	0.948	0.950
*Estimated x[cm]	123.25	124.27	126.54
Exact x[cm]	122	124	124
*Estimated y[cm]	35.72	36.7	38.15
Exact y[cm]	36.42	36.42	37.9
*Estimated Area[cm^2]	13.98	34.81	45.46
Exact Area [cm^2]	12	24	48

*The estimated values of location, and area, are determined as centroid and area of $\overline{\Gamma}_{\gamma}(x, y)$.

TABLE IV. Corrosion location and area estimation for each simulated corrosion case.

Corrosion Stage	I	II	III
$\bar{V}$[m/sec]	2785.8	2702.5	2714.1
Estimated remnant Thickness [mm]	1.58	1.40	1.42
Exact Remnant Thickness [mm]	1.26±0.1	1.26±0.1	1.26±0.1

TABLE V. Thickness loss estimation for each simulated corrosion case.

Belanger and Cawley [16] demonstrated that if the damage size is smaller than the width of the first Fresnel zone the area of the damage can be overestimated using the A_0 mode. This problem is due to scattering effects that causes erroneous time delay in the wave packets of rays (helical paths in the vicinity of the corrosion patch) that do not cross the corrosion patch. These time delays

will appear in the objective function of Eq. (19) and compromise the estimation of the corrosion boundary. Table V shows the estimated wave velocities and the associated remnant thicknesses for the three simulated corrosion patches. The remnant thicknesses are slightly underestimated. Again, as it was shown in [16], this error is most likely caused by the violation of the ray theory related to the Fresnel zone. It is worth noting that, although the imaging method exploited here was the MHUI, other imaging algorithms could be adapted in the same fashion to quantify damage using the image information.

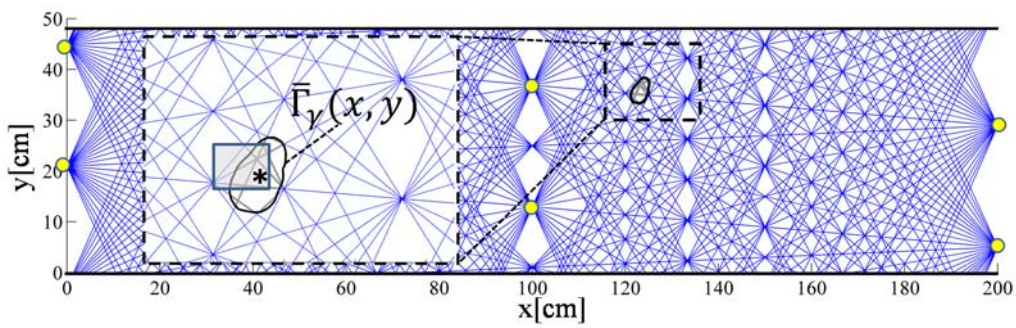

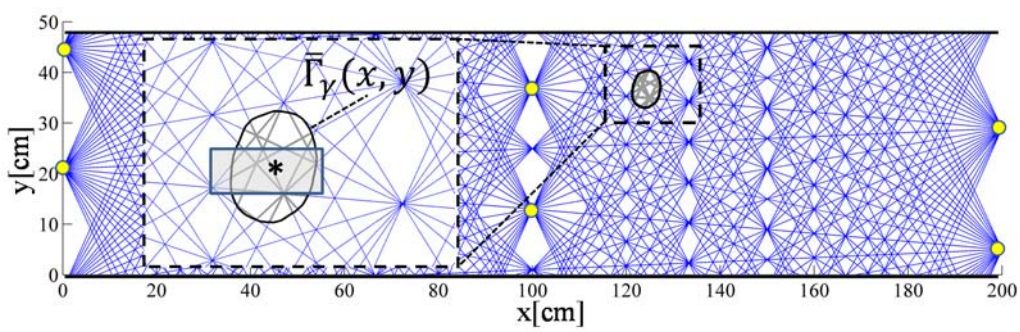

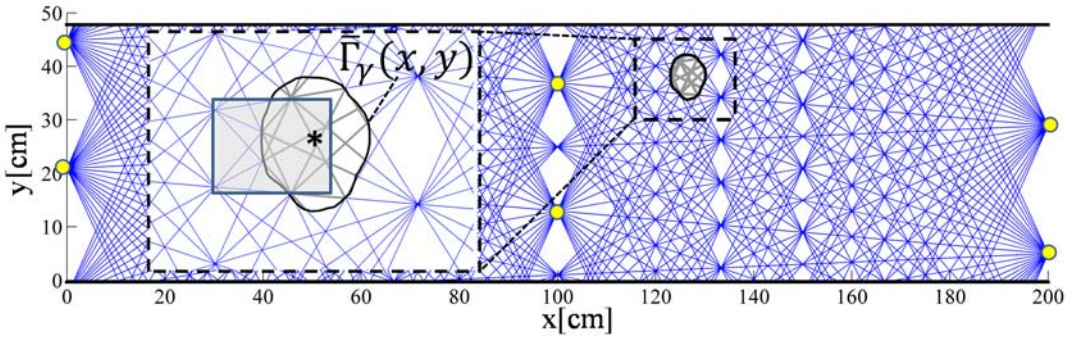

FIG. 25 Quantitative corrosion patch monitoring results for damage cases I, II, and III.

2.4. Summary

This section has successfully demonstrated the application of a multi helical ultrasonic imaging (MHUI) algorithm for monitoring cylindrical structures. The MHUI exploits the fact that, since there are infinitely many helical paths between a pair of transducers, a theoretically infinite amount data can be extracted from each signal. Extracting more data associated with multiple helical paths enables multiple lines to be inspected between a single transducer pair, instead of only a single line, as is traditionally done.

The main challenge of the proposed approach is the feature extraction, which depends on two parameters, namely, the relative position of transducer pairs and the wave velocity. Guidelines were suggested to fully exploit the benefits of the proposed approach. Specifically, a separation coefficient was presented to properly design the sensor network. In addition, in order to overcome limitations due to the multimode nature and dispersive behavior of Lamb waves, the excitation frequency was selected in a frequency range below the first cut-off frequency (i.e., where only the two fundamental Lamb wave modes can propagate), and in a frequency range in which A_0 and S_0 group wave velocities are less dispersive. Experimental results demonstrated the good performance of the proposed approach. Although the contribution of higher Lamb modes was not considered here, they could be included by using more sophisticated signal processing algorithms.

The MHUI method has also been extended to generate quantitative information about the corrosion patch, including location, size and remnant thickness. The proposed approach consisted of two

main stages. In the first stage, the image information was provided by the MHUI. In the second stage, image corrosion characteristics were estimated by solving an optimization problem. The main advantage of the proposed method is the ability to exploit qualitative image information in order to quantify the extent of the corrosion damage using a low density sensor network. Experiments were carried out on a steel pipe instrumented with six permanently attached piezoelectric disks to validate the approach. Three thickness recesses simulating a growing corrosion patch were considered. Results demonstrated that the proposed method successfully estimates the location, corrosion area, and remnant thickness with reasonable accuracy, while using a small number of sensors.

3. ACOUSTIC EMISSION LOCALIZATION

3.1. Overview

Acoustic emission (AE) is a term that describes the excitation of vibration (sound) waves due to an impulse (e.g. impact, internal fracture). The excitation of ultrasonic waves due to an acoustic emission event has been used in the nondestructive testing field as a means of triangulating its source location.

In contrast to the active methods presented earlier, which are used for estimating the extent and location of corrosion patches, a passive method is applied to localize an acoustic emission source. Whereas, in the active method, signals are sent and received between transducer pairs, in the passive method signals are only received. The task is then one of using knowledge of the waveguide, sensor locations, and received signals to estimate of the location that the disturbance originated from. In a sense, the transducers “listen” for signs of an acoustic emission.

In this section, a similar sensor layout compared to that presented earlier is used to detect simulated acoustic emission events on a steel pipeline. The excited waves propagate in the same helical fashion around the structure, and this fact is exploited during the triangulation phase. Uncertainties in the measurements are also considered, and these sources of error are propagated through a

localization algorithm in order to estimate uncertainty in the final estimation for the acoustic emission source location.

3.2. Source Localization in Cylindrical Shells

3.2.1. Geodesic analysis

The shortest of the helical paths taken by any wave mode corresponds to its first arrival at a sensor. In analyzing the first arriving wave mode at a sensor, possible candidates for the shortest path from the source to a given sensor are evaluated, and the shortest is elected as the "geodesic". For an isotropic medium, the geodesic (shortest path) is equivalent to the path of minimum energy [22]. For a cylindrical shell subjected to an acoustic emission event (pictured in Fig. 26), the representation of its "unwrapped plate" equivalent is contained in Fig. 27.

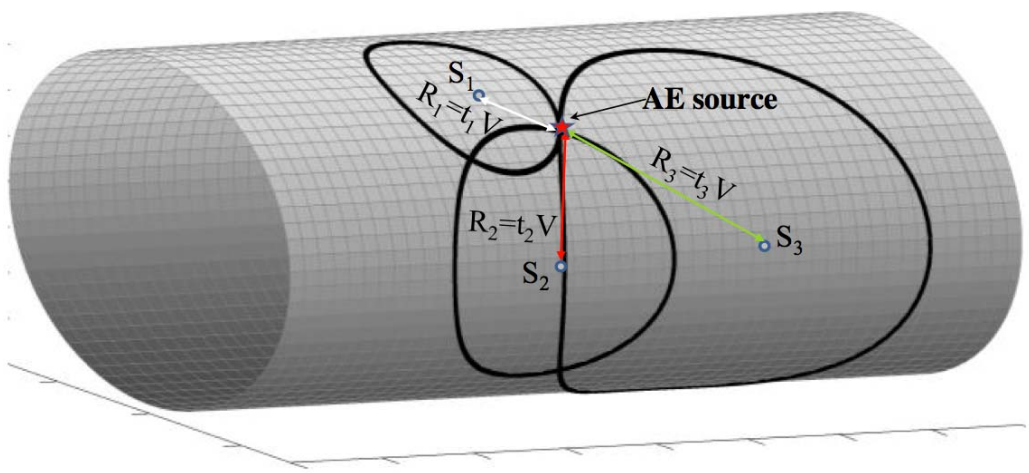

FIG. 26 Triangulation of an acoustic emission source in a cylindrical shell using three sensors.

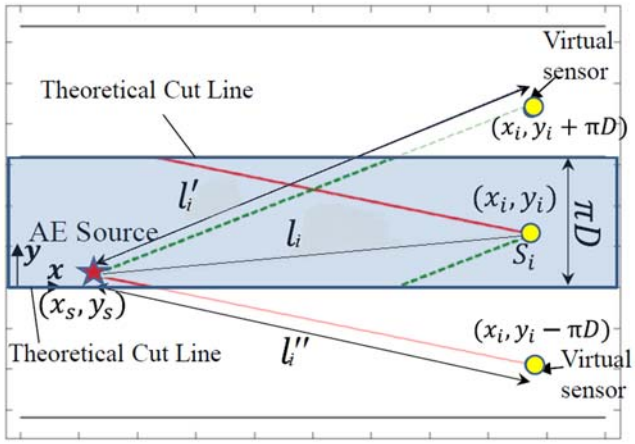

FIG. 27 Unwrapped view representation of the outer pipe surface.

Under this representation, paths that travel along different directions of the cylinder circumference may now be viewed as propagating toward a "virtual" sensor whose circumferential coordinate is $\pm n\pi D$ relative to the actual location. Examples of this may be seen in Fig. 27. For a given source, the geodesic, L_i, is chosen from the argument of $\min\{\ell_i, \ell_i', \ell_i''\}$, with the three possible geodesic candidates contained within. The problem may now be stated as an attempt to find the source location that produces a length for each sensor satisfying the distance required from the input time and velocity information.

The first received signal at a sensor (designated the master, m) is used as a reference for computing the lag in arrival time, Δt_i, at the remaining i sensors. Including knowledge of the mean wave velocity, v, an estimate of the AE source location is possible, through the selection of the source coordinate (x_s, y_s) yielding the closest approximation to the following relation

$$v\Delta t_i = L_i - L_m\,, \quad \text{for } i = 1,2,\ldots,(N-1) \tag{21}$$

where N is the number of sensors used in the triangulation algorithm, including the master sensor. The geodesic lengths are a function of both the trial source and the known sensor locations.

Assuming error-free reception of ideal signals at each sensor, a minimum of three sensors is required for triangulation of the AE source. However, as there is error involved in these measurements, the addition of a fourth aids in minimizing the predicted zone of the source. Furthermore, as an exact solution to the problem will likely not be found, the algorithm for determining the estimation of the AE source location now becomes based on the minimization of the error between a trial estimation and the measured data. This is formulated as an optimization problem, applied to the weighted square of residual errors, and expressed as follows

$$J\left(x_s, y_s\right) = \left(\tilde{Z} - Z\right) R^{-1} \left(\tilde{Z} - Z\right)^T \tag{22}$$

where $J(\cdot)$ is the function to be minimized, the measurement vector $\tilde{Z}$ contains measured differential times, $\Delta\tilde{t}_i$, and the trial vector Z contains theoretical differential times, Δt_i , corresponding to each tested (x_s,y_s) pair. The weighting matrix, R^{-1}, is the inverse of the error covariance matrix for the measurement of time differences,

$$R = \begin{bmatrix} \sigma^2_{\Delta t,1} & \cdots & 0 \\ \vdots & \ddots & \vdots \\ 0 & \cdots & \sigma^2_{\Delta t,(N-1)} \end{bmatrix} \tag{23}$$

where $\sigma^2_{\Delta t,i} = \sigma^2_{t,i} + \sigma^2_{t,m}$. In order to predict this variance in time, the arrival times of the signal at each sensor are assumed to be mutually independent Gaussian random variables, each with individual variance, $\sigma^2_{\Delta t,i}$, with the index applied accordingly. The variance in wave velocity, σ^2_v , is determined experimentally, and is discussed in a later section.

The optimization problem defined in Eq. (22) is in general non-convex. Several algorithms have been developed in the literature for solving this kind of problem, such as Genetic Algorithms (GA) [26,27], Particle Swarm Optimization (PSO) [28], and Mesh Grid Optimization (MGO) [29]. In

this paper, a MGO algorithm is used, with 1 mm resolution in both the x and y directions. Therefore, the AE source coordinates (x_s, y_s) are estimated by evaluating the objective function of Eq. (22) at gridded locations on the unwrapped cylindrical surface. The resulting absolute minimum value of the objective function represents the estimated source location. The overall localization algorithm proposed here is shown in Fig. 28.

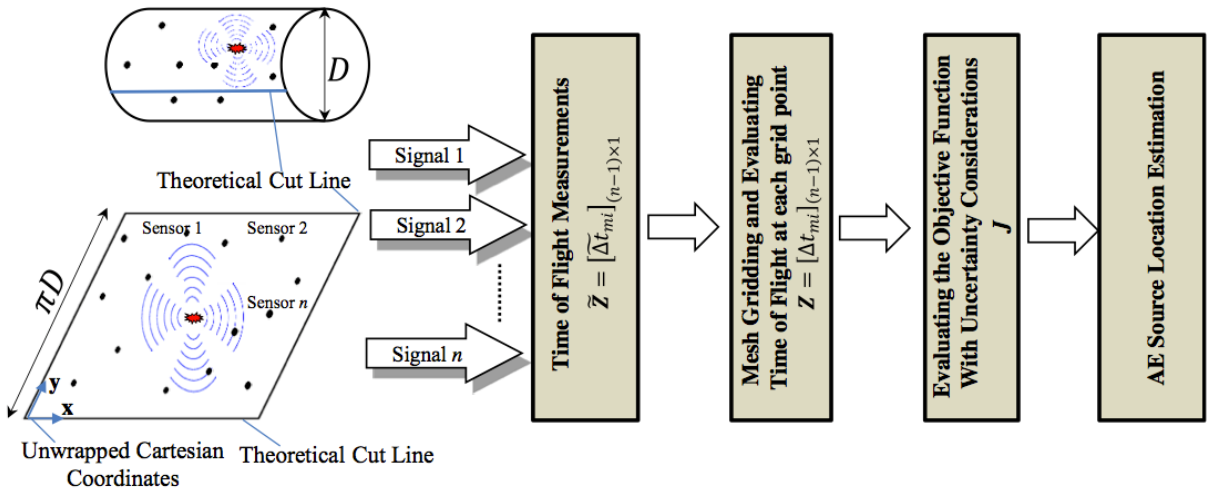

FIG. 28 AE source localization sequence.

3.2.2. Time-of-flight measurement

The time-of-flight is recorded for the discrete signal received at each sensor by the method of threshold crossing. This is a simple approach with minimal computation, and it is commonly used in methods of AE source localization [23], [24]. The motivation for choosing threshold crossing in determining the time-of-flight of the first arriving wave mode here, instead of an alternative method like cross-correlation, is a result of the geometry of the cylinder. In the presence of multiple helical paths for a single mode, there is the possibility for interference between a mode traveling along different paths and arriving at a single sensor at roughly the same moment in time. The resulting distortion of the mode shape thus introduces complications to the method of signal correlation, which has the potential for generating poor time-of-flight estimations.

An appropriate threshold level for time-of-flight is determined upon the level of noise present in the signal. The signal is first processed through a bandpass filter to eliminate the low-frequency, high amplitude components that are present, which are mainly due to the highly dispersive nature of the flexural mode. The threshold is then applied to the envelope, $s_A[k]$, of the filtered real discrete signal, $s[k]$, which is formed by obtaining the magnitude of its analytic representation

$$s_A[k] = \| s[k] + i\hat{s}[k] \| \tag{24}$$

where $\hat{s}[k]$ is the discrete Hilbert transform of the real signal.

Time-of-flight measurement of a discrete signal by this method introduces a systematic error, however, arising from the requirement of the signal envelope to exceed the given threshold amplitude at a certain finite sample point. The time-of-flight recorded by this method, for instance, may be some $\tilde{t}$, which is higher than the true time-of-flight, t, by a small amount $\varepsilon_t \leq (1/f_s)$, where f_s is sampling frequency. Because of this, the variance in a single time measurement, $\sigma^2_{t,i}$, may be approximated to $(1/f_s)^2$. The time-of-flight measurement is recorded at each sensor in an identical manner, and thus the variance in differential time, $\sigma^2_{\Delta t,i}$, is defined as twice the individual, $2(1/f_s)^2$ [25]. This systematic uncertainty on the measurement of time is the sole consideration of error for this parameter.

3.3. Probability Zone Determination of AE Source

3.3.1. Uncertainty propagation based on Unscented Transform

As time-of-flight data and information on wave velocity is to be used for the prediction of the AE source location, a method of translating their uncertainties into an uncertainty in the location must now be suggested. The method used in this paper is the Unscented Transform (UT). Unlike the Extended Kalman Filter [14, 17], the UT method avoids the need of linearizing the model. The

method realizes a more appropriate algorithm for capturing the nonlinearity of the proposed source location technique.

The transform consists of creating a number of sigma points, χ, and weighting factors, w, from the mean and variance of the measured data. Each of these sigma points is used to make a prediction for the AE source location. This is accomplished by subjecting each sigma point to the optimization function, J, and returning an estimated source location for each instance.

For each AE simulation, its associated source estimations, $\Psi = \{(x_s,y_s)_0, \ldots, (x_s,y_s)_{2N}\}$, are used to create the mean of this estimate as

$$\left(\bar{x}_s, \bar{y}_s\right) = \sum_{n=0}^{2N} w_n \Psi_n \tag{25}$$

where $(\bar{x}_s, \bar{y}_s)$ is the predicted mean location. The covariance between the two coordinates is now expressed in matrix form as

$$P = \sum_{n=0}^{2N} w_n \left(\Psi_n - \left(\bar{x}_s, \bar{y}_s\right)\right)\left(\Psi_n - \left(\bar{x}_s, \bar{y}_s\right)\right)^T \tag{26}$$

The two parameters introduced above are now used to create a bivariate Gaussian probability distribution, $p(x_s,y_s)$, associated with the estimation of the AE source location, as

$$p\left(x_s, y_s\right) = \frac{1}{\sqrt{(2\pi)^2 |P|}} \exp\left[\frac{1}{2}\Delta\left(\begin{bmatrix} x_s \\ y_s \end{bmatrix}, \begin{bmatrix} \bar{x}_s \\ \bar{y}_s \end{bmatrix}, P\right)\right] \tag{27}$$

where $\Delta(\ )$ is the operator that returns the Mahalanobis distance, δ, from the point (x_s, y_s) to the mean $(\bar{x}_s, \bar{y}_s)$, subject to the covariance P.

3.3.2. Confidence quantification

As a particular Mahalanobis distance, δ, is uniquely associated with a certain confidence level, α, a unique confidence ellipse that quantifies the accuracy of the estimated source location may be now formed. The Mahalanobis distance is distributed according to the chi-square distribution, with two degrees of freedom, as this distance is the result of two Gaussian random variables, wherein

$$\delta - \left(\begin{bmatrix} x_s \\ y_s \end{bmatrix} - \begin{bmatrix} \bar{x}_s \\ \bar{y}_s \end{bmatrix} \right) P^{-1} \left(\begin{bmatrix} x_s \\ y_s \end{bmatrix} - \begin{bmatrix} \bar{x}_s \\ \bar{y}_s \end{bmatrix} \right)^T = 0 \tag{28}$$

The above formulation describes an ellipse centered about the mean location estimate, which is dependent upon the value of δ. Thus, in order to create a unique ellipse based upon a certain confidence level, a relation between the Mahalanobis distance and the confidence is now introduced. As δ follows the chi-square distribution, it may be expressed in terms of the proportion α, a certain amount of the probability distribution enclosed, as

$$\delta = -2\ln(1-\alpha) \tag{29}$$

Specifying a certain level of confidence in α may now be equated to forming an ellipse about the mean of the AE source prediction.

3.3.3. Numerical evaluation

In order to quantitatively evaluate the AE distribution obtained by the Unscented Transform, the Kullback-Leibler divergence (D_{KL}) is used compare the results to a Monte Carlo simulation. In

probability theory the D_{KL} is a measure of the difference between two probability distributions. The D_{KL} for two continuous probability distributions $p(x)$ and $q(x)$ is defined as [36]:

$$D_{KL}(p \square q) = \int_{-\infty}^{+\infty} p(x) \ln\left(\frac{p(x)}{q(x)}\right) dx \tag{30}$$

where x is a random variable. The D_{KL} is a non-symmetric and non-negative value. It is equal to zero if and only if $p(x) = q(x)$ almost everywhere.

The D_{KL} between two bivariate Gaussian distributions resulting from the UT and Monte Carlo can be calculated as:

$$\begin{aligned} & D_{KL}\left(\begin{bmatrix} x_s \\ y_s \end{bmatrix}_{UT} \square \begin{bmatrix} x_s \\ y_s \end{bmatrix}_{MC}\right) \\ & = \frac{1}{2}\left(tr\left(\boldsymbol{P}_{MC}^{-1}\boldsymbol{P}_{UT}\right) + \left(\begin{bmatrix} \bar{x}_s \\ \bar{y}_s \end{bmatrix}_{MC} - \begin{bmatrix} \bar{x}_s \\ \bar{y}_s \end{bmatrix}_{UT}\right)^T \boldsymbol{P}_{MC}^{-1}\left(\begin{bmatrix} \bar{x}_s \\ \bar{y}_s \end{bmatrix}_{MC} - \begin{bmatrix} \bar{x}_s \\ \bar{y}_s \end{bmatrix}_{UT}\right) - 2 - \ln\left(\frac{\det(\boldsymbol{P}_{UT})}{\det(\boldsymbol{P}_{MC})}\right)\right) \end{aligned} \tag{31}$$

where $\begin{bmatrix} \bar{x}_s \\ \bar{y}_s \end{bmatrix}_{UT}$, $\begin{bmatrix} \bar{x}_s \\ \bar{y}_s \end{bmatrix}_{MC}$, $\boldsymbol{P}_{UT}$, and $\boldsymbol{P}_{MC}$ are the mean estimated locations and covariance matrices for each of the two distributions (UT and Monte Carlo), respectively.

The qualitative differences between a UT algorithm and a traditional Monte Carlo simulation are shown in Figs. 29 and 30. The UT method uses fewer sample points than the Monte Carlo method. Using UT a distribution is representatively sampled while using the fewest number of sample points. This allows for a large reduction in computation time, without sacrificing accuracy.

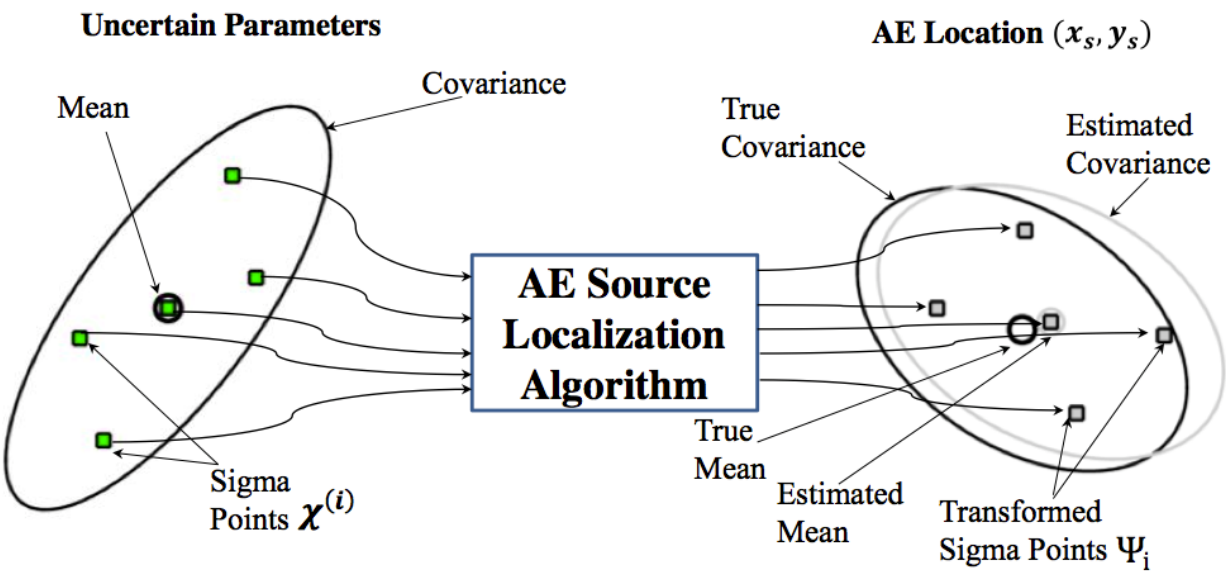

FIG. 29 Visualization of the Unscented Transform sampling algorithm.

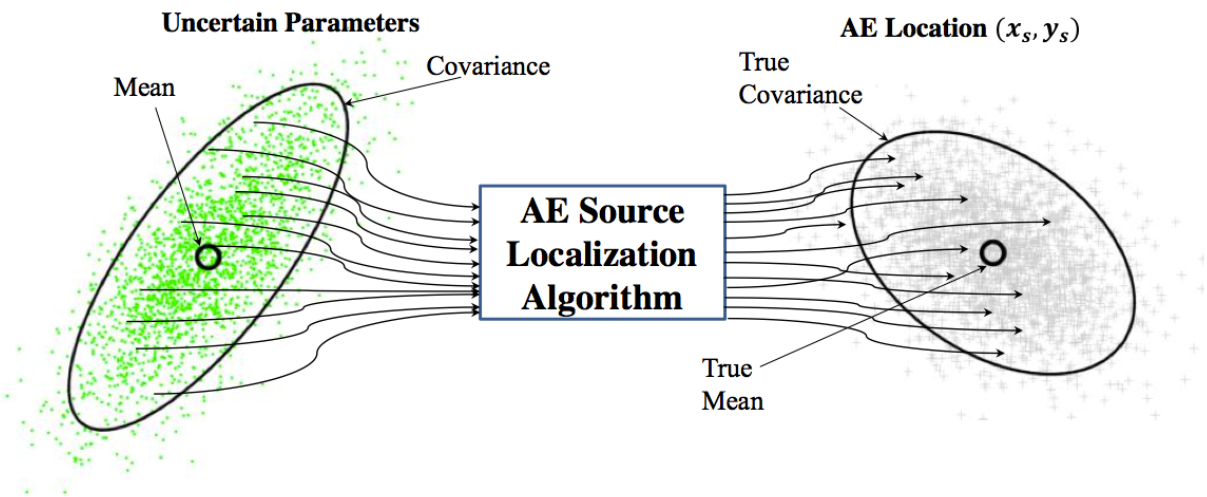

FIG. 30 Monte Carlo simulation using a statistically significant number of sample points.

3.4. Experimental Testing

3.4.1. Setup of experiment

In order to validate the effectiveness of the proposed algorithm, experiments were carried out using a 3 m long steel pipe, with a diameter of 15.24 cm and a wall thickness of 2.1 mm. The pipe was

instrumented with an array of six piezoelectric transducer disks. These are arranged in longitudinal groups of two along the pipe. The outer surface of the pipe specimen was gridded both longitudinally and circumferentially at 40 mm and in one-eighth increments of the pipe circumference, respectively. Fig. 31 may be referenced for further details regarding the setup.

Each transducer was connected to a 40 dB preamplifier. The system included an eight channel high-speed data acquisition board (Physical Acoustics Corporation Micro-II PAC) with a 3 MHz sampling frequency and dedicated software (AEwin) for signal processing and data storage. Post-processing of the received AE signals was performed with a PC running a MATLAB code implemented by the authors.

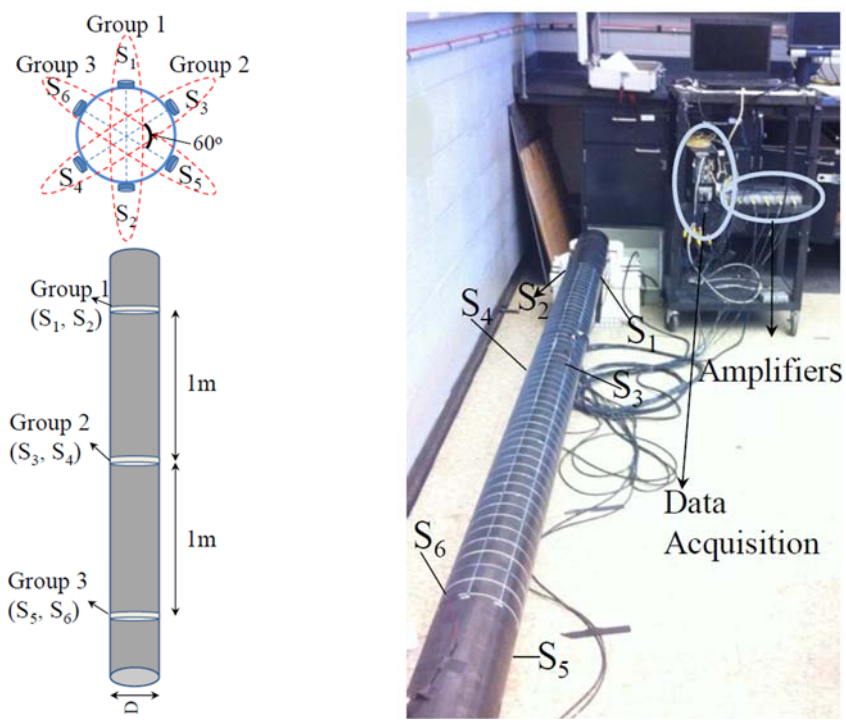

FIG. 31 Arrangement of transducer sensors (left), and pipe and layout of processing tools (right).

The input statistics for wave velocity were measured using pencil lead breaks on the pipe surface at known locations on the grid. A total of 183 wave velocities were measured for the S_0–like extensional mode. The mean, v, and standard deviation, σ_v , were found to be 5277 m/s and 244 m/s, respectively.

3.4.2. Results

AE sources were generated at eleven locations on the grid of the pipe (see Fig. 32). For each source location, the first four triggered sensors were used as input for the measurement time data. This translates into using only those sensors that are closest to the AE source, reducing the area of the pipe that must be tested for possible source locations. The mesh grid for the trial source locations was spaced at 1 mm increments in both the x and y coordinates.

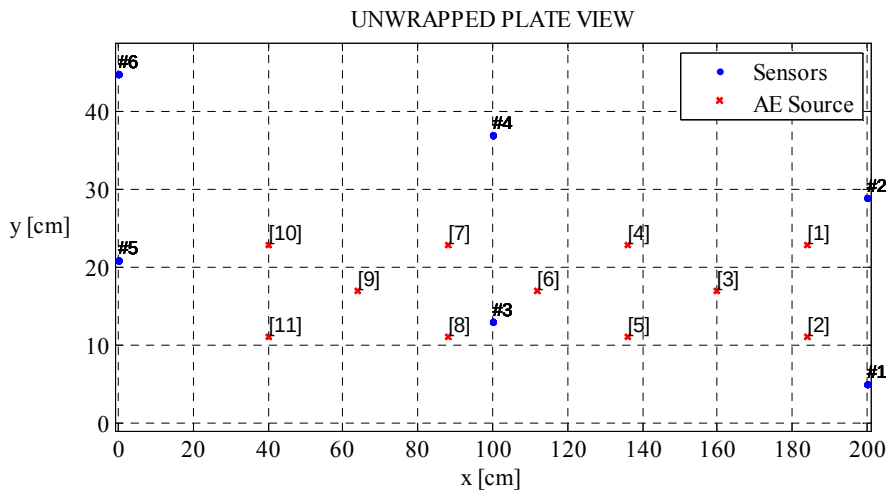

FIG. 32 Layout of sensor locations on the unwrapped grid view of the pipe surface.

AE simulation #1 may serve as an example. Results for the input mean and variance data for the Unscented Transform associated with this simulation are summarized in Eq. (32).

$$\overline{X} = \begin{bmatrix} \left[\Delta\tilde{t}_i\right]_{(N-1)} \\ v \end{bmatrix} = \begin{bmatrix} 13.66\,\mu\text{s} \\ 125.7\,\mu\text{s} \\ 127.0\,\mu\text{s} \\ 5277\text{ m/s} \end{bmatrix} \qquad P_X = \text{diag}\left\{\left(\frac{1}{3\text{E}6}\text{ s}\right)^2, \ldots, \left(\frac{1}{3\text{E}6}\text{ s}\right)^2, (244\text{ m/s})^2\right\} \tag{32}$$

where P_x is a diagonal matrix of dimension four. With four samples of input data, nine sigma points are generated using the UT algorithm. Both these and their corresponding weights are summarized in Table VI.

Sigma Point	χ_0	χ_1	χ_2	χ_3	χ_4	χ_5	χ_6	χ_7	χ_8
$\widetilde{\Delta t}_1$ [μs]	13.66	14.60	13.66	13.66	13.66	12.72	13.66	13.66	13.66
$\widetilde{\Delta t}_2$ [μs]	125.7	125.7	126.6	125.7	125.7	125.7	124.7	125.7	125.7
$\widetilde{\Delta t}_3$ [μs]	127.0	127.0	127.0	127.9	127.0	127.0	127.0	126.1	127.0
v [m/s]	5277	5277	5277	5277	5763	5277	5277	5277	4791
w_i	0	0.125	0.125	0.125	0.125	0.125	0.125	0.125	0.125

TABLE VI. Results of propagating input time and velocity data into the UT algorithm.

The above 2N+1 sigma points are then processed through the optimization function to produce 2N+1 AE source location estimates. Fig. 33 shows the results of the AE source prediction algorithm for 11 different simulated locations along the pipe surface, each enclosed by the corresponding 90% probability mass.

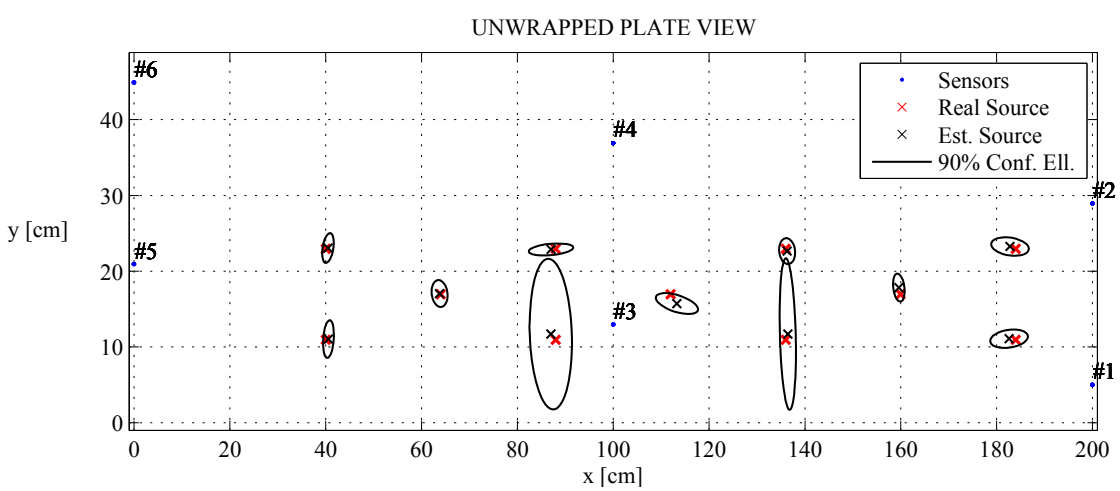

FIG. 33 Plots of mean estimates and 90% confidence ellipses for 11 simulated AE sources.

The above results show excellent agreement in both the error in distance between the estimated mean and the actual source location, as well as in the 90% probability density mass, in each instance enclosing the real source within.

However, a spreading of the ellipses about the pipe circumference may be seen for a small number of the estimated source locations, namely AE sources #5 and #8. In these cases, although the single order Gaussian distribution about the estimated mean encompasses each estimated location, this is not a rigorous prediction of the uncertainty. This is due to the fact that the circumferential spreading is caused by a small number of input sigma points whose values have differed sufficiently from the input mean; enough to trigger the election of a different helical path as the geodesic for at least one of the sensors. The resulting minimum of the optimization function is thus shifted circumferentially in order to match such a variation from the input mean. An emphasis of this phenomenon for AE source #8 is shown in Fig. 34.

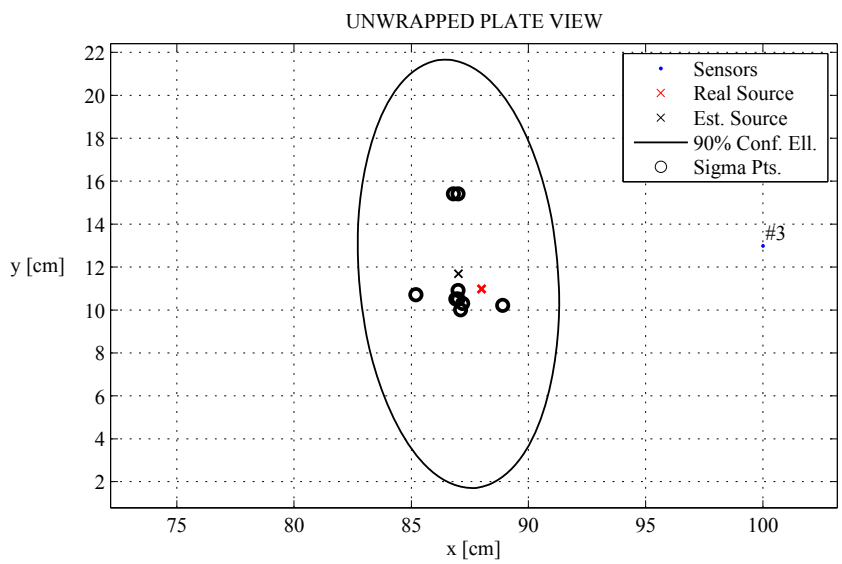

FIG. 34 Enhanced image of the estimation components for AE source #8.

In this figure, two of the nine sigma points satisfying different helical paths for sensors #4 and #6 may have undergone a shift in the circumferential position.

Physically, the possibility of two unique helical paths, simultaneously producing the same arriving mode at the same instant in time is not possible. Thus, a more rigorous estimation of uncertainty

in these cases would be a bimodal distribution focused about two different estimated locations. This further detailing of the probability distribution, however, is not fully considered here. It is important to note in Fig. 34 that the unimodal Gaussian distribution still provides a good estimate of the actual source location. The shortcoming only involves the shape of the 90% confidence ellipse when the true distribution is bimodal.

The Kullback-Leibler divergence is applied to the 11 AE simulations to compare the UT method to a traditional Monte Carlo simulation. Fig. 35 presents the D_{KL} value for each of the 11 AE locations. The Monte Carlo results are assumed to represent the true distribution for each AE location, due to statistical significance of the large sample size that is used. The low values for the D_{KL} demonstrate the similarity between the results of the UT and Monte Carlo methods. When interpreting the values, it is important to note that if the two resulting distributions (UT and Monte Carlo) were identical, the D_{KL} value would be zero. Thus, the lower the value, the closer the two distributions are. The UT method thus generates a distribution for the AE source location that is statistically similar to the "true" distribution, which is found using a large number of sample points. However, the UT algorithm requires much less computation time, as its sample points are fewer in number and representatively chosen.

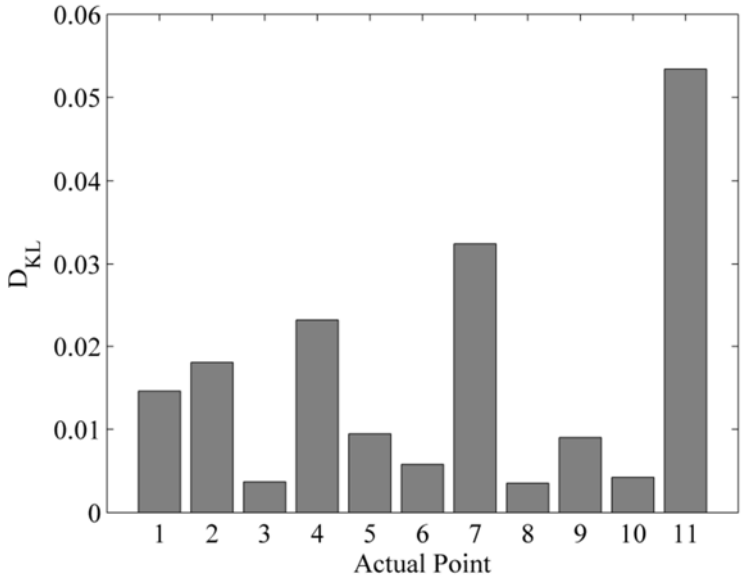

FIG. 35 Kullback-Leibler divergence for each AE location, comparing the UT method to a Monte Carlo simulation.

3.5. Summary

Traditionally, AE source localization is performed by assuming the source location to be a deterministic quantity. Instead of solving for a point estimate of the source location, a probability distribution for the source location is presented here, based on uncertainty in time-of-flight and wave velocity measurements. Thus, the source location is assumed to be a random vector with total uncertainty characterized by the probability distribution function.

Here, an approach based on the Unscented Transform (UT) was presented to estimate the mean and covariance of the AE source location distribution. To evaluate the performance of the UT method, Monte Carlo simulations were also carried out, and a Kullback-Leibler divergence was used to statistically compare the results of each. It was shown that UT was able to accurately estimate the mean and covariance of the AE location using a smaller set of samples than the Monte Carlo simulations. The accuracy of the proposed framework demonstrated its potential application in real-time SHM applications. However, more formal tests need to be conducted to verify the robustness of the approach to more practical defect and damage types, such as cracks, and corrosion.

4. BROADER IMPACTS

One graduate student (PhD) and two undergraduate students have worked on this project as full-time research assistants. In addition, the PI integrated the results of this project into an existing graduate course in structural health monitoring (CIE 680 Structural Health Monitoring and Nondestructive Evaluation). As a requirement for this course, students have to investigate during the semester a topic selected by the instructor. At the end of the semester students have to teach a lecture on the assigned topic. This lecture should contain a minimum of five major sections including: introduction, fundamental concepts, instrumentation, applications and conclusions. During the Fall 2013 a group of three graduate students worked on a topic entitled “Structural Health Monitoring of Corrosion in Oil Pipelines”. Students carried out a detailed literature review on the current procedures to assess corrosion damage. Fig. 36 shows the first slide of the group’s presentation at the end of the semester.

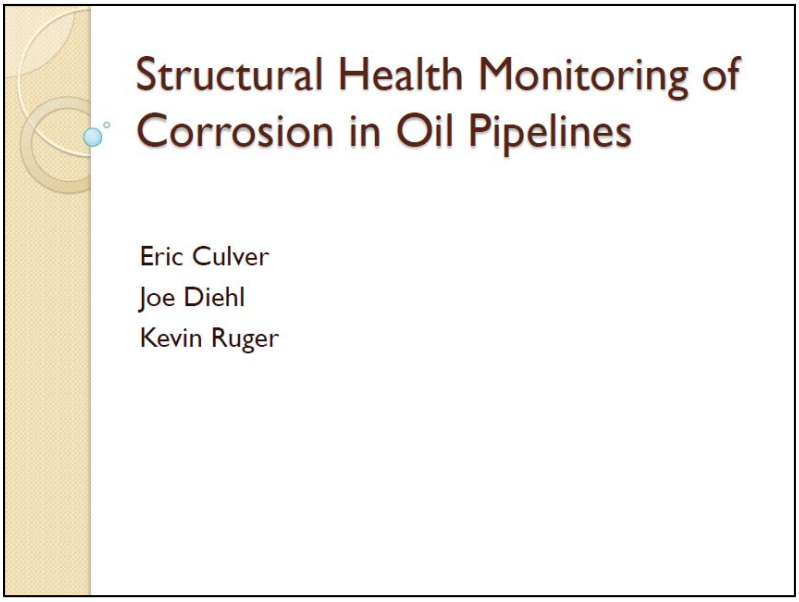

FIG. 36 CIE 680 project presentation slide.

Over the last two years the results from the activities of the research have been included in two journal papers:

- Dehghan Niri, E., Salamone, S., (2015). "A multi-helical ultrasonic imaging approach for the structural health monitoring of cylindrical structures", Structural Heath Monitoring: an international Journal, Vol. 14(1), pp.73-85.
- Dehghan Niri, E., Matovu, M., Salamone, S., (2016). "Quantitative corrosion imaging of pipelines using multi helical guided ultrasonic waves", Structural Control and Health Monitoring, under review.

and three conference presentations:

- Dubuc, B., Dehghan Niri, E., Farhidzadeh, A., Salamone, S., (2015). "Multi-helical ultrasonic imaging for corrosion monitoring of cylindrical structures", Proceedings of SPIE's: Health Monitoring of Structural and Biological Systems, San Diego, CA, March 8-12.
- Dehghan Niri, E., Ebrahimkhanlou, A., Dubuc, B., Salamone, S., (2015). "Multi-Helical Acoustic Emission Damage Localization for Corrosion Monitoring of Cylindrical Structures", ASNT 24th Research Symposium, Anaheim, CA, March 16-19.
- Dehghan Niri, E., Farhidzadeh, A., Salamone, S., (2014). "Multi-mode (passive-active) real time corrosion and leak monitoring of cylindrical structures", Proceedings of 23rd ASNT research symposium, 24-27 March 2014, Minneapolis, MN, USA.

5. CONCLUSIONS

This project has investigated the use of a built-in monitoring system based on permanently installed low profile piezoelectric transducers which have the capability of transmitting and receiving guided ultrasonic waves (GUWs) over the length of a pipeline. Advanced signal processing algorithms based on probabilistic concepts have been developed to perform the critical tasks of: 1) damage localization (e.g., leaks), and 2) damage characterization (e.g., thickness map).

Thickness mapping has been achived by a multi helical ultrasonic imaging (MHUI) algorithm. The MHUI exploits the fact that, since there are infinitely many helical paths between a pair of transducers, theoretically an infinite amount data can be extracted from each received signal. Extracting more data associated with multiple helical paths from a received signal enables multiple lines to be inspected between a single transducer pair instead of only a single line, as is traditionally inspected between two transducers. The main challenge of the proposed approach is the feature extraction, which depends on two parameters, namely, the relative position of transducers pairs, and the wave velocity. Guidelines have been suggested to fully exploit the benefits of the proposed approach. Specifically, a separation coefficient was presented to properly design the sensor network. In addition, in order to overcome limitations due to the multimode nature and dispersive behavior of Lamb waves, the excitation frequency should be selected in a frequency range below the first cut-off frequency (i.e., where only the two fundamental Lamb wave modes A_0 and S_0 can propagate), and in a frequency range in which A_0 and S_0 group wave velocities were less dispersive. Experimental results have demonstrated the good performance of the proposed approach. Although the contribution of the higher Lamb modes was not considered here, they could be included by using more sophisticated signal processing algorithms. In addition, leaks are monitored as Acoustic Emission (AE) events by detecting the waves generated in the pipe. Traditionally, AE source localization is performed assuming the source location, to be a deterministic quantity. Instead in the proposed approach the source location is assumed to be a random vector with total uncertainty characterized by the probability distribution function. An approach based on Unscented Transformation (UT) has been demsotrated to estimate the mean and covariance of the AE source location distribution. To evaluate the performance of UT, Monte Carlo simulations has been carried out, and a Kullback-Leibler divergence has been used. It is

shown that UT has been able to accurately estimate the mean and covariance of the AE location using a set of samples smaller than the Monte Carlo simulations. The accuracy of the proposed framework demonstrated its potential application in real-time SHM applications. However, more formal tests need to be conducted to verify the robustness of the approach to more practical defect and damage types, such as cracks, corrosion, etc.

6. REFERENCES

[1] P. B. Nagy, F. Simonetti, and G. Instanes, "Corrosion and erosion monitoring in plates and pipes using constant group velocity Lamb wave inspection," *Ultrasonics*, vol. 54, no. 7, pp. 1832–1841, 2014.

[2] P. Cawley, F. B. Cegla, and M. Stone, "Corrosion monitoring strategies: Choice between area and point measurements," *J. Nondestruct. Eval.*, vol. 32, pp. 156–163, 2013.

[3] C. L. Willey, F. Simonetti, P. B. Nagy, and G. Instanes, "Guided wave tomography of pipes with high-order helical modes," *NDT E Int.*, vol. 65, pp. 8–21, 2014.

[4] M. K. Hinders and E. V. Malyarenko, "Contact scanning Lamb wave tomography," *J. Acoust. Soc. Am.*, vol. 104, no. 1790–1791, 1998.

[5] K. R. Leonard and M. K. Hinders, "Guided wave helical ultrasonic tomography of pipes," *J. Acoust. Soc. Am.*, vol. 114, no. 2, p. 767, 2003.

[6] K. R. Leonard and M. K. Hinders, "Lamb wave tomography of pipe-like structures," *Ultrasonics*, vol. 43, no. 7, pp. 574–83, Jun. 2005.

[7] J. Li and J. L. Rose, "Natural beam focusing of non-axisymmetric guided waves in large-diameter pipes," *Ultrasonics*, vol. 44, no. 1, pp. 35–45, Jan. 2006.

[8] P. Huthwaite and F. Simonetti, "High-resolution guided wave tomography," *Wave Motion*, vol. 50, pp. 979–993, 2013.

[9] A. D. Pierce and H. G. Kil, "Elastic wave propagation from point excitations on thin-walled cylindrical shells," *J. Vib. Acoust.*, vol. 112, no. 89, pp. 399–406, 1990.

[10] D. J. Yoon, Y. H. Kim, and O. Y. Kwon, "New Algorithm for Acoustic Emission Source Location in Cylindrical Structures," *J. Acoust. Emiss.*, vol. 9, pp. 237–242, 1992.

[11] X. Zhao, H. Gao, G. Zhang, B. Ayhan, F. Yan, C. Kwan, and J. L. Rose, "Active health monitoring of an aircraft wing with embedded piezoelectric sensor/actuator network: I.

Defect detection, localization and growth monitoring," *Smart Mater. Struct.*, vol. 16, pp. 1208–1217, 2007.

[12] T. R. Hay, R. L. Royer, H. Gao, X. Zhao, and J. L. Rose, "A comparison of embedded sensor Lamb wave ultrasonic tomography approaches for material loss detection," *Smart Mater. Struct.*, vol. 15, pp. 946–951, 2006.

[13] E. V. Malyarenko and M. K. Hinders, "Ultrasonic Lamb wave diffraction tomography," *Ultrasonics*, vol. 39, pp. 269–281, 2001.

[14] A. Moustafa and S. Salamone, "Fractal dimension-based Lamb wave tomography algorithm for damage detection in plate-like structures," *J. Intell. Mater. Syst. Struct.*, vol. 23, pp. 1269–1276, 2012.

[15] A. Bagheri, K. Li, and P. Rizzo, "Reference-free damage detection by means of wavelet transform and empirical mode decomposition applied to Lamb waves," *J. Intell. Mater. Syst. Struct.*, vol. 24, no. 194–208, 2013.

[16] P. Belanger and P. Cawley, "Feasibility of low frequency straight-ray guided wave tomography," *NDT E Int.*, vol. 42, no. 2, pp. 113–119, Mar. 2009.

[17] J. Hou, K. R. Leonard, and M. K. Hinders, "Multi-mode Lamb wave arrival time extraction for improved tomographic reconstruction," *Inverse Probl.*, vol. 20, pp. 1873–1888, 2004.

[18] P. Belanger, "Feasibility of thickness mapping using ultrasonic guided waves," Imperial College London, 2009.

[19] P. Belanger and P. Cawley, "Lamb wave tomography to evaluate the maximum depth of corrosion patches," *AIP Conf. Proc.*, vol. 975, no. 1, 2008.

[20] E. Dehghan-Niri, S. M. Zahrai, and A. Mohtat, "Effectiveness-robustness objectives in MTMD system design: An evolutionary optimal design methodology," *Struct. Control Heal. Monit.*, vol. 17, pp. 218–236, 2010.

[21] T. G. Kolda, R. M. Lewis, and V. Torczon, "Optimization by Direct Search: New Perspectives on Some Classical and Modern Methods," *SIAM Rev.*, vol. 45, no. 3, pp. 385–482, Jan. 2003.

[22] R. Gangadharan, G. Prasanna, M. R. Bhat, C. R. L. Murthy, and S. Gopalakrishnan, "Acoustic emission source location and damage detection in a metallic structure using a graph-theory-based geodesic approach," *Smart Mater. Struct.*, vol. 18, no. 11, p. 115022, Nov. 2009.

[23] P. Nivesrangsan, J. A. Steel, and R. L. Reuben, "Source location of acoustic emission in diesel engines," *Mech. Syst. Signal Process.*, vol. 21, no. 2, pp. 1103–1114, Feb. 2007.

[24] T. Kundu, S. Das, and K. V. Jata, “Detection of the point of impact on a stiffened plate by the acoustic emission technique,” *Smart Mater. Struct.*, vol. 18, no. 3, Mar. 2009.

[25] J. Minkoff, *Signal processing fundamentals and applications for communications and sensing systems*. Norwood, MA: Artech House, 2002.

[26] S. Julier, J. Uhlmann, and H. F. Durrant-Whyte, “A New Method for the Nonlinear Transformation of Means nd Covariances in Filters and Estimators,” *IEEE Trans. Automat. Contr.*, vol. 45, no. 3, pp. 477–482, 2000.